Automation, Surgery Support and Intuitive 3D visualization
to optimize workflow in image guided therapy SysTems

DELIVERABLE D7.3

Public report of project results

Project number:	ITEA 20044
Document version no.:	v1.0
Edited by:	Ernst Hermens, Robert Hofsink
Date:	14.09.2024

ITEA Roadmap challenge:
Smart Health

HISTORY

Document version #	Date	Remarks
V0.1	24.02.2022	Starting version, template
V0.2	14.04.2024	First version started from D1.1, scope was adjusted
V0.3	29.08.2024	Input provided by Innova
V0.4	06.09/2024	Integration and review of all use cases
V1.0	14.09.2024	Final version

Deliverable review procedure:

- **2 weeks before due date**: deliverable owner sends deliverable –approved by WP leader– to Project Manager
- **Upfront** PM assigns a co-reviewer from the PMT group to cross check the deliverable
- **1 week before due date**: co-reviewer provides input to deliverable owner
- **Due date:** deliverable owner sends the final version of the deliverable to PM and co-reviewer

TABLE OF CONTENTS

1 Introduction

This document provides a description of the updated State of the Art for the clinical disease areas addressed in the ASSIST project. The goal of ASSIST is to develop technologies and solutions that provide support for diagnosis, treatment planning, image visualization and treatment execution. Typically, the developed solutions are data driven and heavily rely on Artificial Intelligence as the discriminating factor to deliver improvements in terms of speed and accuracy of diagnosis and better treatment outcome.

Five clinical procedures are addressed so that it is possible to discriminate between common aspects of (in-)efficiencies for these disease areas and specific ones:

- Intracranial hemorrhage
- Brain oncology
- Lung oncology
- Hepato Pancreato Billiary oncology
- Prostate enlargement

This deliverable D7.3 builds further on D1.1 which already provided short descriptions of the abovementioned disease areas and their clinical procedures, summarizing existing workflow steps and bottlenecks. For each disease area a section is added, describing the advancements made in the ASSIST project for that particular area.

2 Clinical disease areas

2.1 Intracranial haemorrhage

Owner: Innova – Tufan Dogan

2.1.1 Introduction

Intracranial hemorrhage refers to any bleeding within the intracranial vault, including the brain parenchyma and surrounding meningeal spaces (Caceres, 2012). Acute intracranial hemorrhage (ICH) is a potentially life-threatening condition that requires fast and accurate detection because of its frequently rapid progression during the first several hours.

ICH could be caused by various reasons ranging from trauma, vascular disease to congenital development (Ye, 2019). Hypertension and Cerebral amyloid angiopathy are the most common causes of hemorrhagic stroke. Cigarette smoking and moderate or heavy alcohol consumption, diabetes mellitus, chronic liver disease, decreased low-density lipoprotein cholesterol and low triglycerides are other important risk factors (Unnithan AKA, 2022). Severe headache, loss of consciousness, vomiting, neck stiffness increases in blood pressure are neurological symptoms often associated with intracranial hemorrhage. (Burduja, 2020) (Unnithan AKA, 2022)

The age-standardized incidence of stroke in Europe ranged from 95 to 290/100,000 per year and absolute number of stroke cases is expected to reach 1.5 million per year in 2025 cases (Béjot, 2016). Haemorrhagic stroke contributes to 10% to 20% of strokes annually (Unnithan AKA, 2022). However, it is deadlier, with a reported case fatality ratio of 24–37% at 7 days and 40–59% at 30 days (Qdaisat, 2022)

The costs of hospitalization for stroke are also high and differed substantially by types of strokes. Due to frequent imaging and surgical intervention, patients admitted with intracranial haemorrhage have the potential to account for significant costs. Fernando et al (2018) found that the mean total cost for intracranial patients was C$75,869 and the mean cost per day for intracranial hemorrhage patients was C$3,994. (Fernando, 2018) The estimated US national cost was $12.55 billion for intracerebral haemorrhage ICH-related hospitalization in 2011–2012 and mean cost per person for hospitalization is $24,077 and monthly 3-year homecare cost is $14,487 in the United States (Yousufuddin, 2020).

2.1.2 Clinical state of the art

Intracranial hemorrhage (ICH), a subtype of stroke, can be classified into five sub-types according to bleeding location: Intraventricular (IVH), Intraparenchymal (IPH), Subarachnoid (SAH), Epidural (EDH) and Subdural (SDH). The ICH that occurs within the brain issue is called UnHemorrhage (Figure 1). Although ICH is less frequent than ischemic stroke, it presents a higher mortality rate. The degrees of severity and interventions vary with bleeding types (Ye, 2019).

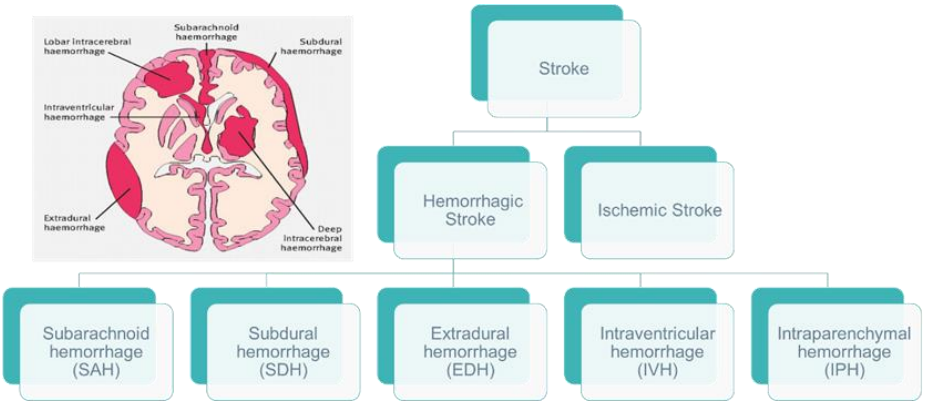

Figure 1 Sub-types of strokes and hemorrhagic strokes

Emergency treatment differs for hemorrhagic and ischemic strokes. In ischemic strokes, emergency IV medication and emergency endovascular procedures are options to restore blow flood to the brain quickly. Carotid endarterectomy, angioplasty and stents are other procedures to decrease risk of having another stroke. However, emergency treatment of hemorrhagic stroke focuses on controlling the bleeding and reducing pressure in the brain. Emergency measures, surgery, surgical clipping, coiling, surgical arteriovenous malformation removal and stereotactic radiosurgery are treatment options for hemorrhagic strokes (Clinic).

Classification of ICH and distinguishing it from ischemic stroke is critical due to prompt appropriate treatment and mitigate neurological deficit, and mortality. In ischemic strokes, therapy with drugs that can break up a clot has to be given within 4.5 hours from when symptoms first started if given intravenously. Intravenous tissue-type plasminogen activator (IV-tPA) is the gold standard treatment for ischemic stroke. It improves outcomes in ischemic stroke but is associated with certain risks such as potential bleeding in the brain. Differentiating extradural hemorrhage from subdural (SDH) hemorrhage in the head is also important. While extradural hemorrhage is treated with expedient evacuation via a craniotomy, SDH has various management strategies depending on the size, location and extent of mass effect.

Non-contrast Computed Tomography scan is usually the first imaging method used to assess patients with suspected ICH and distinguish ICH from ischemic stroke as it can be performed fast and has high sensitivity for hemorrhage. Hemorrhage and its sub-types can be recognized on non-contrast CT since blood has slightly higher density (Figure 2). CT scans generate a sequence of images using X-ray beams. Depending on the amount of tissue X-ray absorbency, brain tissues are captured with different intensities. CT scans are displayed using a windowing method. Different features of the brain tissues can be displayed in the grayscale image by selecting different window parameters. In the CT scan images, the ICH regions appear as hyperdense regions with a relatively undefined structure (Hssayeni, 2020). However, there are difficulties in using CT scan to detect hemorrhages due to their similar appearance with parenchyma and complexity in distinguishing mass effect and edema (Mirza, 2017). Even highly trained experts may miss subtle life-threatening findings, and many hospitals do not have trained neuro-radiologists, especially at night and on weekends.

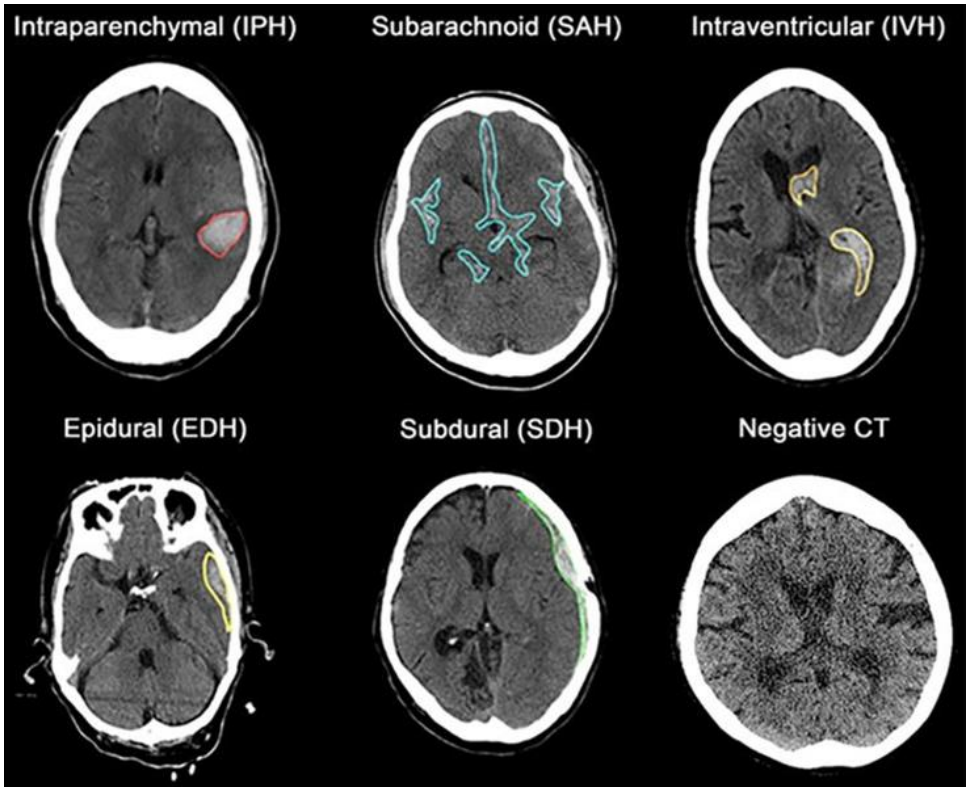

Figure 2 Non-contrast Computed Tomography scans for ICH sub-types. Note. Reprinted from (Kim, 2021)

Although acute stroke is one of the most common causes of disability worldwide and numbers are projected to increase, timely access to modern treatments is most often restricted to urban populations, particularly those living in rural and remote areas. Figure 3 illustrates the workflow for a stroke patient being transferred from a rural facility to a regional hospital center. At this workflow, interpretation of CT images has highest priority.

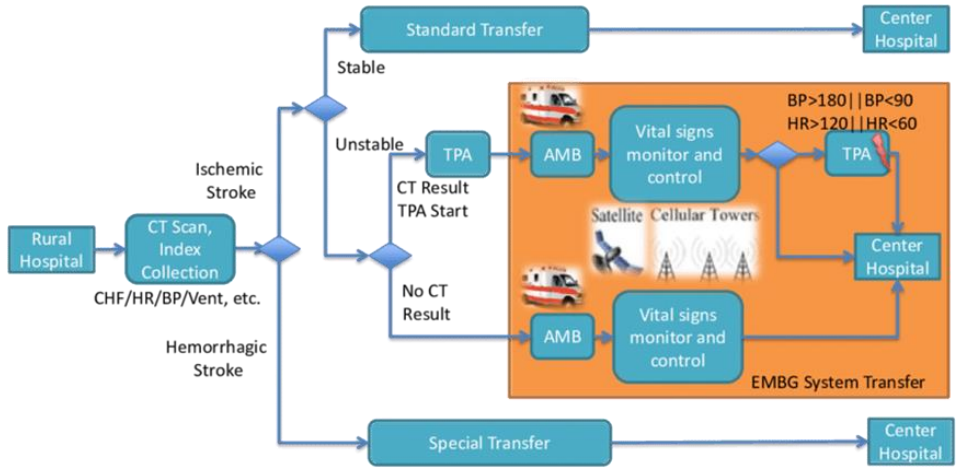

Figure 3 Clinical workflow for stroke patient care from a rural hospital to a regional center hospital. Note. Reprinted from "A Mobile Geo-Communication Dataset for Physiology-Aware DASH in Rural Ambulance Transport. Proceedings of the 8th ACM on Multimedia Systems Conference" (Hosseini, 2017)

2.1.3 Workflow inefficiencies and bottlenecks

The main challenges in ICU diagnosis and treatment are shown in Table 1. A system that identifies intracranial hemorrhage with high accuracy comparable to experts has a great potential to help reduce mortality rates and costs. The system that allows the medical staff in the emergency department in rural area for triaging an acute stroke patient who may be eligible for tissue-type plasminogen activator can not only improves your chances of survival but also may reduce complication. A tool for expeditious and accurate diagnosis of ICHs may facilitate a prompt therapeutic response and ultimately improved outcomes. Recent advances in deep convolutional neural networks have showed that the method has a great potential in automating ICH detection and segmentation and can assist junior radiology trainees when experts are not available. The automated triage system for accurate ICH detection is also desirable to reduce the rate of misdiagnosis.

Table 1: (Burduja, 2020) (Patel, 2019) (Hssayeni, 2020) (Unnithan AKA, 2022) (Ye, 2019)

Category	Challenge
Interpretation difficulty of non-contrast CT images	Image noise, artefacts and cerebral parenchyma with similar appearance and density make segmentation of ICH challenging
	Differentiating extradural (EDH) from subdural (SDH) haemorrhage in the head can be challenging as SDHs are more common and there are a few distinguishing features which are usually reliable
	Irregularity of the hematoma and different stages of clot formation may further contribute to obscure hemorrhage boundaries and internal heterogeneity
	Gray scale images are limited by low signal-to-noise, poor contrast, and a high incidence of image artifacts. A unique challenge is to identify tiny subtle abnormalities in a large 3D volume with near-perfect sensitivity

Lack of resources	In most clinical centers, initial interpretations of head CT is usually provided by junior radiologists, radiology trainees, or emergency physicians and initial interpretations will be reviewed later by senior or more-experienced radiologists. Several studies have confirmed that discrepancies exist between the initial and final interpretations and some misinterpretations might even cause clinical consequences
	Diagnosis process relies on the availability of a subspecialty-trained neuroradiologist, and as a result, could be time inefficient and even inaccurate, especially in remote areas where specialized care is scarce.
Time-consuming decision-making process	The urgency of the procedure, a complex and time-consuming decision-making process, an insufficient level of experience in the case of novice radiologists, and the fact that most emergencies occur at nighttime

2.1.4 Outcomes and project results

The project is mainly focused on the detection and classification of Intracranial Haemorrhages to provide fast and accurate healthcare to patients using deep learning-based technologies with explainability. Synthetic CT generation for epidural haemorrhages, PACS based inference system, deep learning-based ICH detection and classification algorithms and explainable AI results can be considered as the main deliverables, especially for the ICH use case at the end of the project. Moreover, the use case provides insights for each partner and increases the strength of collaboration within the project.

2.1.4.1 Synthetic CT Images for Epidural Haemorrhage

Medical imaging problems often suffer from lack of data or unbalanced datasets. To overcome this challenge, we conducted some experiments to generate synthetic epidural haemorrhage CT images using different architectures and models, including GANs, Diffusion Models, etc. Accordingly, a Diffusion-based model called MedFusion (Müller et al. 2023) has generated the images shown in Figure 4 and had the best FID score of 64.3.

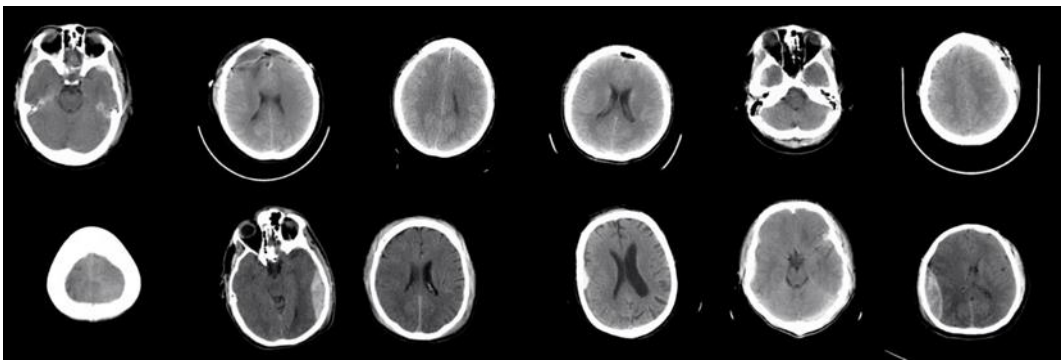

Figure 4 Synthetic CT Images generated by MedFusion

On the other hand, several GAN models including FastGAN (Liu et al. 2020), StyleGan2-ADA (Karras et al. 2020), StyleGan3 (Karras et al. 2021) and CycleGan (Zhu et al. 2017) were tested and experiments showed that the best model for our problem is StyleGan2-ADA. This GAN-based model produced the synthetic images shown in Figure 5 and gave the best result with an FID score of 15.6.

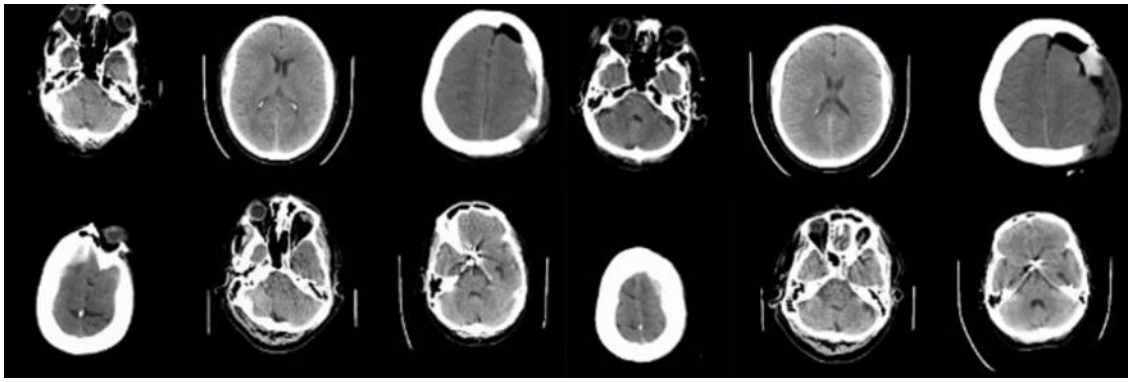

Figure 5 Synthetic CT Images generated by StyleGan2-ADA

As a result, StyleGan2-ADA, pre-trained with the FFHQ dataset, was the best model in terms of performance metrics such as FID and Inception scores. Approximately 3000 synthetic CT images containing epidural haemorrhage were generated using a transfer learning approach. The generated images were used in the training phase of the detection and classification model and improved the model performance by 3% for epidural haemorrhage as shown in the table below.

Table 2: Comparison of ICH classification performance of the model with and without synthetic data in terms of AUC score in training

	AUC Score without Synthetic Data	AUC Score with Synthetic Data	AUC Change (%)
ICH	0,9797	0,9801	0,040828825
EDH	0,9388	0,9711	**3,44056242**
IPH	0,989	0,9887	-0,03033367
IVH	0,9942	0,994	-0,020116677
SAH	0,9729	0,9717	-0,123342584
SDH	0,9696	0,9694	-0,020627063

2.1.4.2 PACS-based Inference System

A PACS-Integrated Inference System which is described in the Figure 6 has been developed to streamline the analysis of radiological images for ICH detection and classification. This system is designed to support three types of end-users, offering flexibility in how they interact with the platform—whether through PACS, RESTful API-

client, or MQTT-client interfaces. It provides both standalone and cloud-based deployment options, ensuring adaptability to various healthcare environments.

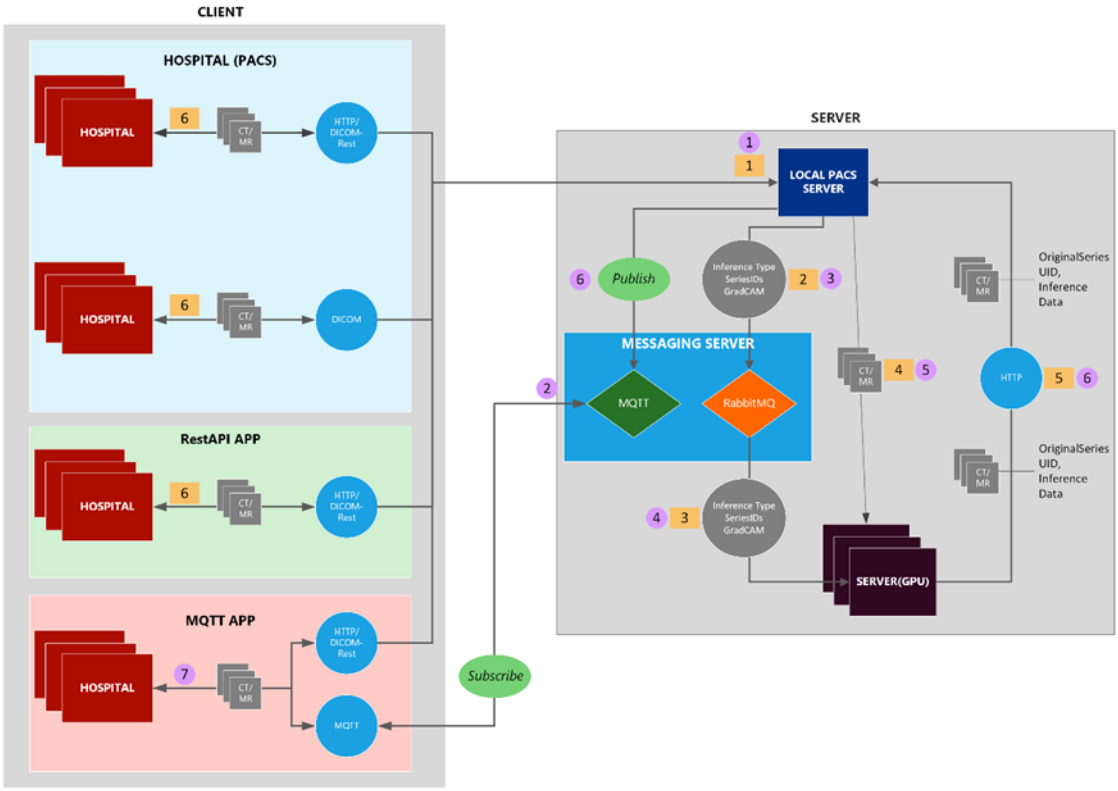

Figure 6 PACS-Integrated Inference System Architecture

The system supports multiple protocols, including DICOM, DICOMweb (STOW, WADO), and HTTP, to guarantee the secure and reliable transfer of DICOM images. End-users can send and receive DICOM images using any of these protocols, benefiting from robust DICOM image storage and management capabilities. The communication framework is built to facilitate seamless interaction between the end-user, the PACS-based Application Server, the Messaging Server, and the Inference (GPU) Server. To enhance processing efficiency, the system offers multithreading support, allowing the inference server to leverage multiple GPUs.

This system is versatile, supporting various DICOM image modalities such as CT and MRI. Once the image analysis is complete, end-users are notified through multiple channels, and they have the option to view, download, or share the analysed images. The platform also offers side-by-side viewing of original and explicable DICOM series, enabling users to easily identify the location of brain haemorrhages. For better organization and searchability, analysed images can be sorted and filtered based on criteria such as Patient ID, Patient Name, and Study Date. Additionally, relevant haemorrhage information is embedded into the DICOM tags with a code string of classification results, enhancing the ease of access to critical data.

The PACS-Integrated Inference System also offers comprehensive support for essential DICOM operations, including upload, storage, and deletion of images. This ensures that users can easily manage their DICOM files within the system, maintaining an organized

and accessible repository of radiological data. Whether adding new images, storing them securely, or removing outdated files, the system provides a streamlined process for all DICOM-related tasks.

A key feature of the system is its flexibility in providing inference options. Users can choose between performing a standard analysis or opting for an analysis that includes explainable AI (XAI) features, all with a single button click. This dual option caters to varying needs, allowing for quick assessments or more detailed examinations with visual explanations that highlight the model's focus during the analysis.

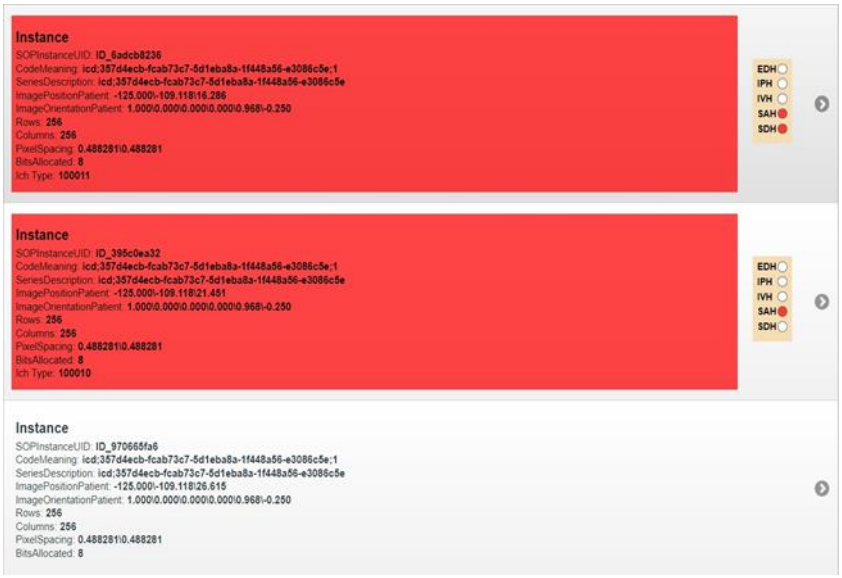

Figure 7 Interface for List of the Inferred Instances

The system is designed with a user-friendly interface that prioritizes ease of use and clarity. The colourful display (in the Figure 7) and organized layout enhance the user experience, featuring clearly marked subtype boxes and intuitive navigation. The side-by-side views in Figure 8 for XAI allow users to compare original and explicable DICOM series effortlessly, making it easier to identify and understand the location and nature of intracranial haemorrhages. Furthermore, the viewer in Figure 9 shows the identified subtype of the slice at the bottom of the image to enhance transparency and user experience. This thoughtful design ensures that healthcare professionals can efficiently interact with the system, improving their workflow and diagnostic accuracy.

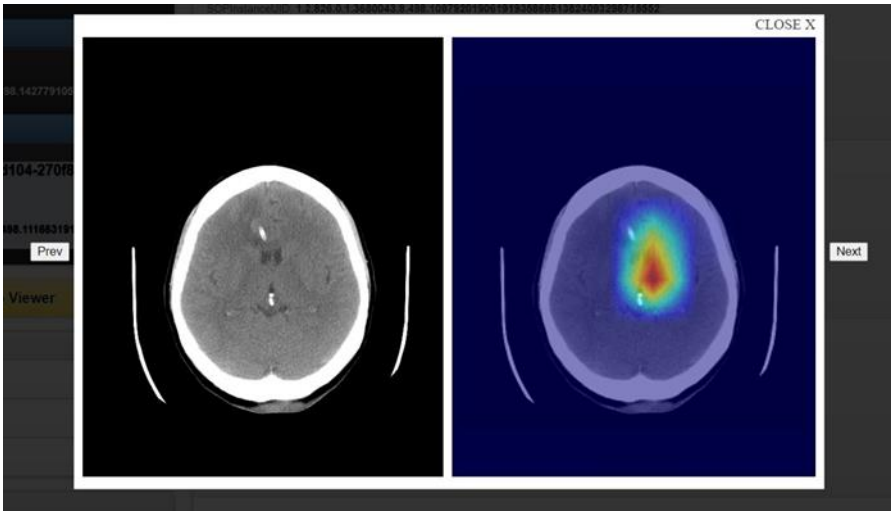

Figure 8 Side-by-side View of Original CT Images and Explainable ICH Results

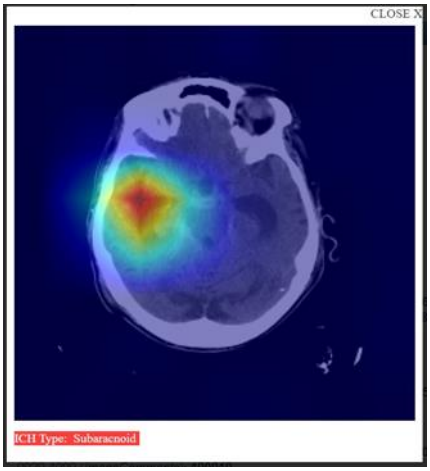

Figure 9 Viewer of the System with Description of Inference

Finally, the PACS-Integrated Inference System is designed for seamless integration with existing clinical workflows, making it an invaluable tool for radiologists and other healthcare professionals in the accurate and efficient diagnosis of ICH.

2.1.4.3 Deep learning-based Explainable ICH Detection and Classification System

A deep learning-based multi layered ICH detection and classification algorithm which can be seen in the Figure 10 has been developed during the project. The approach involves pre-processing medical CT images by combining different window sizes and slice positions, aiming to enhance feature importance in the dataset. The ensemble model developed for ICH detection and classification integrates various deep learning architectures, including Convolutional Neural Networks (CNN), Recurrent Neural Networks (RNN), and Gated Recurrent Units (GRU).

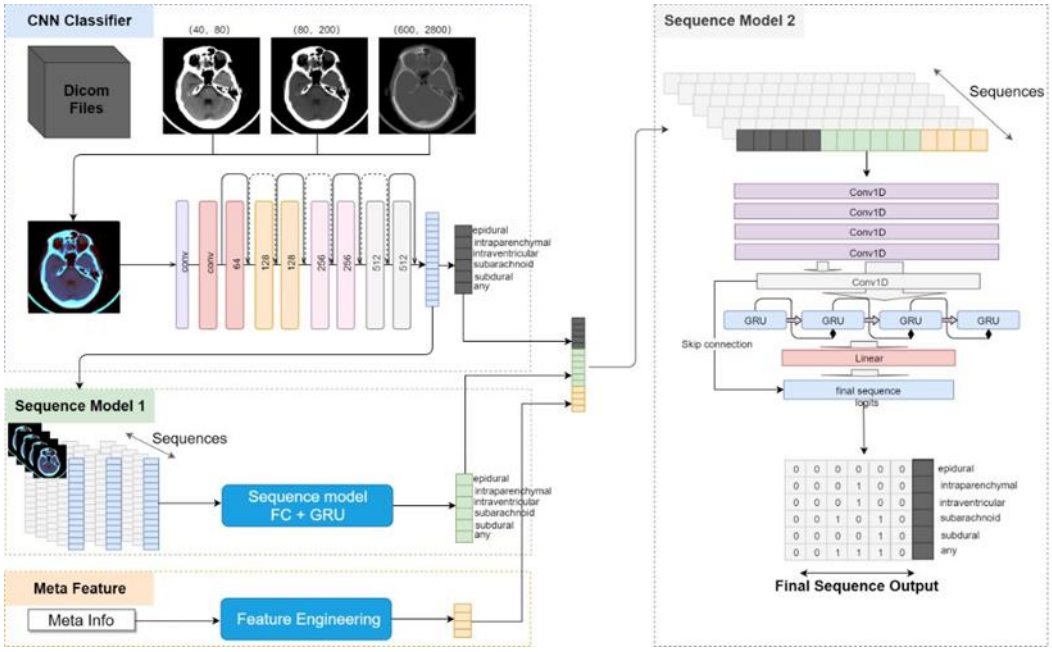

Figure 10 ICH Detection and Classification Model Architecture (Based on Wang et al. 2021)

The CNN model serves as the foundational component of the ensemble framework, focusing on the extraction of high-level features from medical images. In this approach, the SE-ResNeXt101 architecture is employed, which combines the strengths of Squeeze-and-Excitation Networks (SENet) and ResNeXt to enhance feature discrimination and model efficiency. This model is designed to capture complex patterns in the data by processing the images through multiple layers, each layer refining the feature map to better represent the underlying characteristics of ICH. The extracted features from the CNN are not only used for initial classification but also serve as crucial inputs for the subsequent sequence models that further refine the predictions.

Table 3 shows the performance of the model over the test dataset of 78,544 images at the beginning of the project in terms of performance metrics such as accuracy, area under the curve (AUC) and sensitivity, which are crucial for evaluating the model's performance in detecting ICH.

Table 3 CNN-based ICH detection performance in the beginning of the project

	Accuracy	AUC	Sensitivity
ICH Detection	90%	0.92	0.92

Moreover, the model uses two sets of models that aim to mimic the behaviour of expert radiologists, creating links between slices, playing a critical role in refining predictions and improving classification accuracy. The first sequence model which is shown in the Figure 11, takes the feature outputs from the CNN classifier as its input. This model applies a bidirectional-RNN with GRU to generate a refined estimate of the features, enhancing the overall robustness of the feature set before moving on to the next stage.

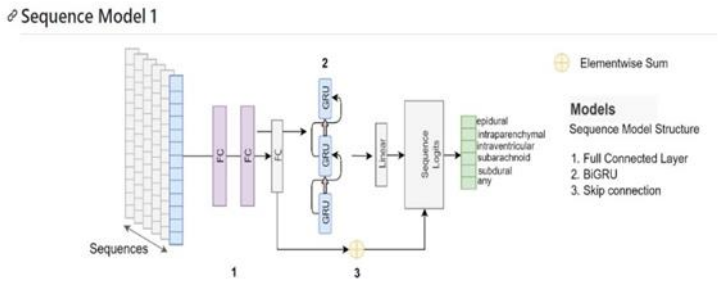

Figure 11 First sequence model architecture (Wang et al. 2021)

The second sequence model which can be seen in the Figure 12, leverages the concept of stacked generalization within the ensemble framework. It uses the GRU-based RNN model to learn how to optimally combine predictions from multiple existing models, effectively synthesizing the strengths of each model to produce more accurate and reliable final classification outputs.

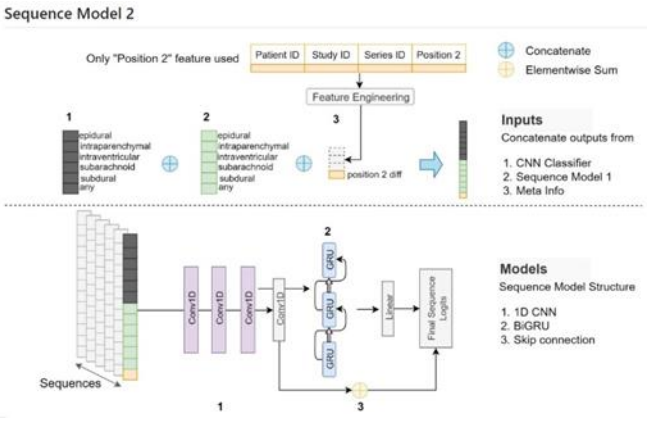

Figure 12 Second sequence model architecture (Wang et al. 2021)

In summary, the approach involves pre-processing medical images by combining different window sizes and slice positions to enhance feature importance. The ensemble model developed for ICH detection and classification integrates CNN, RNN, and GRU to improve detection accuracy.

The classification process begins with a CNN model, specifically the SE-ResNeXt101 architecture, used for feature extraction. The first sequence model refines these features using a bidirectional RNN with GRU units. These refined features, along with those extracted from the CNN and metadata from DICOM tags, are then passed to a second sequence model, which implements stacked generalization to combine predictions from multiple models, leading to final classification. After some experiments on the ensemble model, the accuracy of performance in ICH detection of has been increased by approximately 3% as shown in the Figure 13 below.

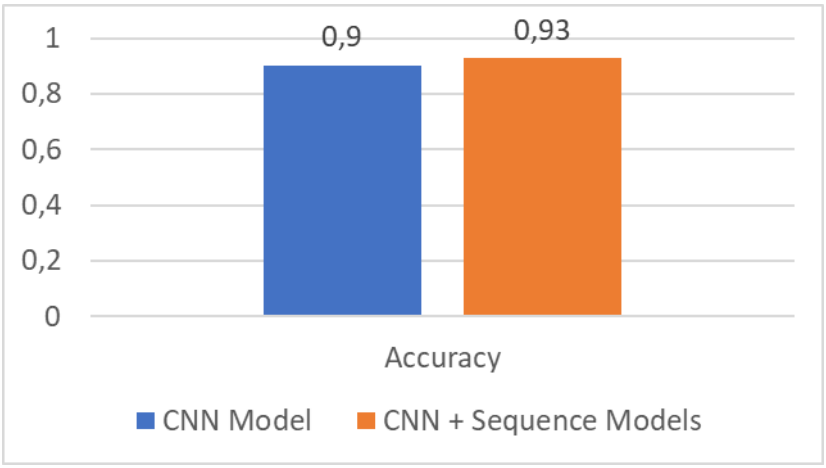

Figure 13 Comparison of model performances in terms of ICH detection accuracy

The ensemble model outputs multiclass classification probabilities, providing predictions for different types of ICH. To enhance interpretability, an explanatory layer is included to visualize which areas of the image the model focuses on during the classification process. Training of the CNN model was conducted using the RSNA 2019 ICH challenge dataset. Various backbones, including SE-ResNeXt101-32x4d and DenseNet-121, were tested with different hyperparameters to identify the optimal configuration for performance. As Table 4 shows, at the end of the project we achieved better ICH detection and classification performance than the scores mentioned earlier.

Table 4 Model performance at the end of the project

	Accuracy	AUC	Sensitivity
ICH Detection	95%	0.94	0.95
Overall Subtype Classification	92%	0.94	0.89

To enhance the interpretability of the model and increase confidence in its predictions, we integrated the Grad-CAM (Gradient-weighted Class Activation Mapping) approach into the ensemble framework. Grad-CAM is an explainable AI technique that highlights the most relevant regions of an image that contribute to the model's decision-making process. By generating visual heat maps, Grad-CAM allows us to see which parts of the image the model is focusing on during classification. These visualizations not only improve the model's explanatory power but also enable radiologists to visually assess the model's focus, providing a clearer understanding of the features that drive its predictions. After improving the model's results, Grad-CAM was tested to ensure that the highlighted regions corresponded accurately to the areas of interest, thereby increasing the reliability and transparency of the model's outputs. A few explainable output examples including different ICH subtypes can be seen in the Figure 14, 15 and 16.

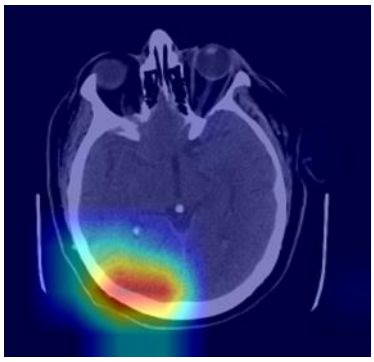

Figure 14 Intraventricular

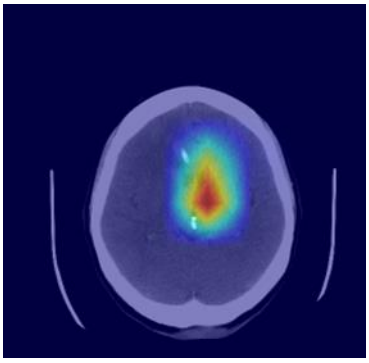

Figure 15 Intraparenchymal

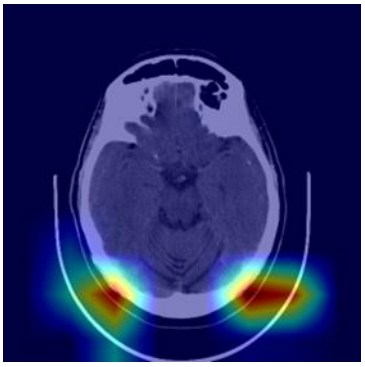

Figure 16 Subdural

Finally, we have developed a system that detects and classifies intracranial haemorrhages (ICH) while providing visual explanations within the ASSIST project. This system seamlessly integrates with a cloud-based inference system which is mentioned above and developed as part of the project. The inference system is DICOM-compatible, scalable, and designed for easy integration. All the components of the system including deep learning models, algorithms, APIs etc. will join Innova's portfolio of health products and strengthen its power in the marketplace.

2.2 Brain tumours

Owner: LiU - Anders Eklund

2.2.1 Introduction

A brain tumor is caused by abnormal cells that form in the brain and is an uncontrolled growth of cells from brain components (primary tumors) or from tumor cells in other areas of the body (metastases). There are hundreds of different types of primary brain tumors with different prognosis and treatment. All types of brain tumors can cause symptoms, which vary depending on which part of the brain is affected. These include headaches, epileptic seizures, vision problems, vomiting, and altered states of consciousness. More specific problems include difficulties with walking, speaking or sensory experiences.

Aside from exposure to vinyl chloride or ionizing radiation, there are no known environmental factors associated with brain tumors. Mutations and deletions of tumor suppressor genes, such as P53, are thought to be the cause of some forms of brain tumor. Inherited conditions, such as Von Hippel–Lindau disease, tuberous sclerosis, multiple endocrine neoplasia, and neurofibromatosis type 2 carry a high risk for the development of brain tumors.

The annual global age-standardized incidence of primary malignant brain tumors is ~3.7 per 100,000 for males and 2.6 per 100,000 for females. Rates appear to be higher more developed countries (males, 5.8 and females, 4.1 per 100,000) than in less developed countries (males 3.0 and females 2.1 per 100,000). In the United States in 2015, approximately 166,039 people were living with brain or other central nervous system tumors. Over 2018, it was projected that there would be 23,880 new cases of brain tumors and 16,830 deaths in 2018 as a result, accounting for 1.4 percent of all cancers and 2.8 percent of all cancer deaths.

There are differences in the incidences of brain cancer in men and women, regardless of the age of those affected. Men are over represented in the incidence of malignant tumors, while women have a higher incidence for non-malignant tumors. There is no consensus within the research community for this disparity.

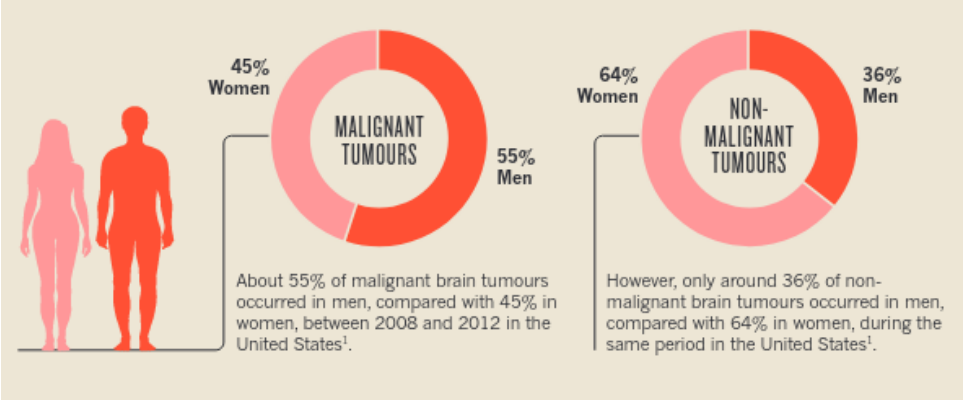

Figure 4 Brain tumor disease characteristics

2.2.2 Clinical state of the art

Most brain tumors are diagnosed after symptoms appear. In general, diagnosing a brain tumor usually begins with magnetic resonance imaging (MRI). Once MRI shows that there is a tumor in the brain, the most common way to determine the type of brain tumor is to look at the results from a sample of tissue after a biopsy or surgery. Brain tumors, when compared to tumors in other areas of the body, pose a challenge for diagnosis. Radioactive tracers that may reach tumors in other areas of the body are unable to reach brain tumors until there was a disruption of the blood-brain barrier (BBB) by the tumor. Disruption of the BBB is well imaged via MRI, and is therefore regarded as the main diagnostic indicator for malignant gliomas, meningiomas, and brain metastases. Other common imaging modalities are CT and/or PET-CT.

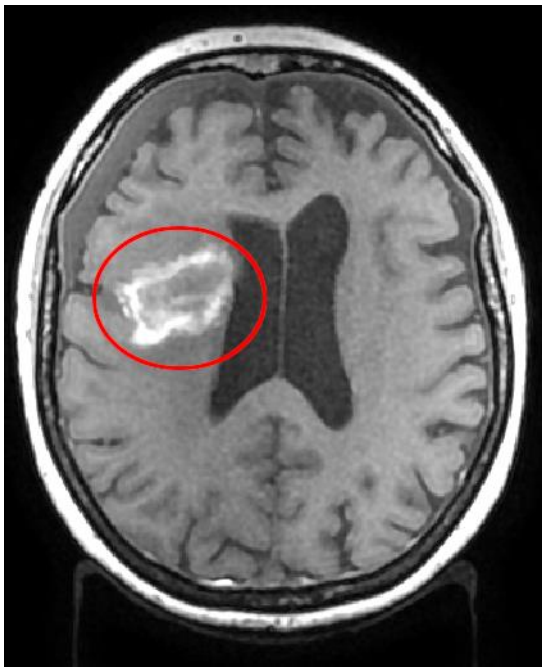

Figure 5 Example brain MRI image

Robotic-assisted brain biopsy is becoming more common, but not considered standard. A robotic probe is the main tool for robot-assisted stereotactic tumor biopsy. It is interfaced with a computerized tomographic (CT) scanner and mounted at its end effector. Once the target is identified, a simple command moves the robot to a position pointing toward the target, which is a faster and more accurate procedure in comparison to the manually adjustable stereotactic frame biopsy. Appropriate preoperative imaging provides an anatomical roadmap to guide the biopsy needle to the exact target

A medical team generally assesses the treatment options and presents them to the person affected and their family. Various types of treatment are available depending on tumor type and location, and may be combined to produce the best chances of survival

2.2.2.1 Surgery

The primary and most desired course of action described in medical literature is surgical removal (resection) via craniotomy. Minimally invasive techniques are becoming the dominant trend in neurosurgical oncology. The main objective of surgery is to remove as many tumor cells as possible, with complete removal being the best outcome and cytoreduction of the tumor otherwise. A Gross Total Resection occurs when all visible signs of the tumor are removed, and subsequent scans show no apparent tumor. In some cases, access to the tumor is impossible and impedes or prohibits surgery.
Many meningiomas, with the exception of some tumors located at the skull base, can be successfully removed surgically. Most pituitary adenomas can be removed surgically, often using a minimally invasive approach through the nasal cavity and skull base (trans-nasal, trans-sphenoidal approach). Large pituitary adenomas require a craniotomy for their removal. Radiotherapy, including stereotactic approaches, is reserved for inoperable cases.

Robot assisted brain tumor resection is a novel filed with and is typically not used in clinical routine.

2.2.2.2 Radiotherapy

Radiotherapy is the most common treatment for secondary brain tumors, but also commonly given as post-surgery for resected tumors in order to further improve local tumor control. Radiotherapy treatment planning is based on CT and/or MRI images, where the MIR images are used to outline the tumor as well as radiosensitive organs at risk (OAR). Delineation of OARs may either be manually or assisted by software. Software based OAR delineation software can either be based on deformation of altases, but AI driven algorithms are becoming the norm. AI delineation of tumor is at the current time a research topic yet to make it into clinical practice.
The most common type of radiation treatment is called external-beam radiation therapy, which typically is directed at a brain tumor in the following ways:

- 3-dimensional conformal radiation therapy (3D-CRT)
  Using images from CT and MRI scans, a 3-dimensional model of the tumor and healthy tissue surrounding the tumor is created. This model can be used to aim the radiation beams directly at the tumor, sparing the healthy tissue from high doses of radiation therapy.
- Intensity modulated radiation therapy (IMRT)
  IMRT is a type of 3D-CRT (see above) that can more directly target a tumor. It can deliver higher doses of radiation to the tumor while giving less to the surrounding healthy tissue. In IMRT, the radiation beams are broken up into smaller beams and the intensity of each of these smaller beams can be changed. This means that the more intense beams, or the beams giving more radiation, can be directed only at the tumor. Volumetric Modulated Arc Therapy (VMAT) is a subset of IMRT involving additional degrees of freedom in treatment delivery.

- Proton therapy
  Proton therapy is a type of external-beam radiation therapy that uses protons rather than x-rays. At high energy, protons can destroy tumor cells. Proton beam therapy is typically used for tumors when less radiation is needed because of the location. This includes tumors that have grown into nearby bone, such as the base of skull, and those near the optic nerve.
- Stereotactic radiosurgery
  Stereotactic radiosurgery is the use of a single, high dose of radiation given directly to the tumor and not healthy tissue. It works best for a tumor that is only in 1 area of the brain and certain noncancerous tumors.

IMRT, VMAT and Proton therapy is an optimization problem, where high tumor dose and low dose to surrounding OAR are conflicting objectives. Recently, AI tools aiming at either creating a treatment plan have emerged and have started to make their way into clinical routine.

2.2.2.3 Chemotherapy

Although chemotherapy may improve overall survival in patients with the most malignant primary brain tumors, it does so in only about 20 percent of patients. Chemotherapy is often used in young children instead of radiation, as radiation may have negative effects on the developing brain. The decision to prescribe this treatment is based on a patient's overall health, type of tumor, and extent of cancer. The toxicity

and many side effects of the drugs, and the uncertain outcome of chemotherapy in brain tumors puts this treatment further down the line of treatment options with surgery and radiation therapy preferred. Additionally, the BBB can prevent some drugs from reaching the cancerous cells.

2.2.3 Workflow inefficiencies and bottlenecks

- Imaging (both MRI and CT) are subjected to noise and artifacts. AI-based reconstruction algorithms have shown promising results, yielding images of higher quality from which diagnosis can be improved. [Diagnosis]
- Since prognosis is heavily linked to tumor progress, the largest benefit to patient outcome would be earlier diagnosis. It is plausible that AI models could play a role here. Research is ongoing in this field. [Diagnosis/Image interpretation]
- To further develop the tools for robot-assisted brain surgery, highly realistic models of the human brain are required — just as animal models of disease are needed to study treatments in patients. Deceased donors are often used to study human anatomy. But in this case, technological development must utilize a model of the brain that begins to bleed when you touch it, has cerebrospinal fluid and allows the conduction of current so that we can stimulate the brain model. [Robotics/Surgery]
- For radiotherapy, multimodal imaging is required, where MRI is used for delineation and CT for treatment planning. This poses a bottle neck as patients' needs to be imaged twice. Image fusion is also required, which adds an additional step. An MRI only workflow, where synthetic CT are generated from MRI and used as a drop-in replacement for CT have begun to become clinically accepted. [Treatment planning/Image fusion]
- The treatment planning process of external beam radiotherapy is time- and resource intensive. AI methods have been proven to yield equal results to manual delineation and planning with none or limited manual interaction. [Treatment planning]

2.2.4 Outcomes and project results

The project has focused on synthetic CT generation, automatic segmentation of tumour and organs at risk, and automatic generation of treatment plans from segmentations, to save time in treatment planning. Another focus has been deep learning for diffusion MRI, for super resolution (Abramian et al., 2023) and for faster analysis of diffusion weighted images that can be informative to fully understand the tumour border (Boito and Özarslan, 2023). All of these applications use deep learning, and a general challenge with deep learning in medical imaging is how to create a large training set. The project has therefore focused on synthetic images (synthetic patients) and federated learning as two ways to make it easier to train deep learning models with large datasets.

Automatic segmentation

Spectronic is a well-established actor in the field of medical imaging with large engagement in both clinical studies and academic scientific work. In the brain use case project we have developed an AI model that performs high quality segmentations of organs at risk in MR images of both brain and head-neck anatomies. The models are developed specifically for radiotherapy planning, where they can both improve and

facilitate the manual steps of identifying and delineating structures that are sensitive to excess irradiation. The developed model has been incorporated in a new product that can be deployed in clinic through the SAINT platform. The AI models and the clinical integration are currently undergoing testing and evaluation together with our clinical research partners. The initial results show that the models perform well on par with manually created delineations, see Figure X and Table X.

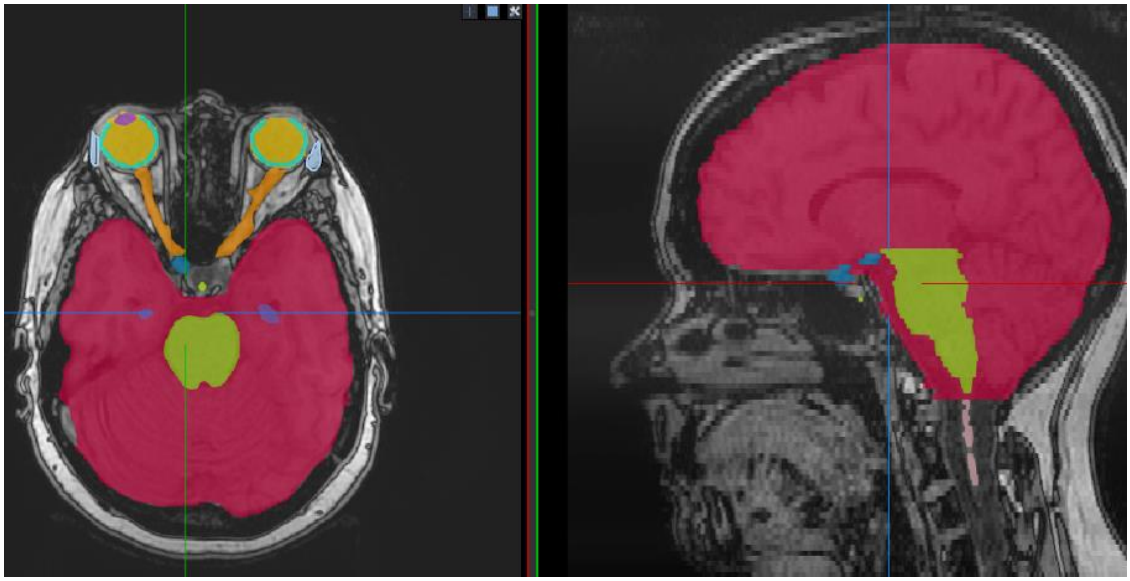

Figure 6 Example image of AI model structure segmentations in brain radiotherapy planning.

Preliminary Dice values of AI model segmentation on 35 patients, compared to manual segmentations.

Pituitary	Lens-L	Lens-R	Eye-L	Eye-R	Chiasm	Optic Nerve-L	Optic Nerve-R	Brain Stem	Brain
0,63	0,56	0,57	0,84	0,82	0,48	0,52	0,50	0,83	0,96

Synthetic brain tumour images

For synthetic image generation, LiU and Eigenvision have demonstrated that GANs (generative adversarial networks) and diffusion models can synthesize realistic brain tumour images and the corresponding annotation of different parts of the tumour. See Figure 5 for examples of real and synthetic brain tumour images. We have also demonstrated that these synthetic images can be used to train segmentation networks with acceptable performance. See Figure 6 for obtained Dice scores when training segmentation networks with real or synthetic images, and testing them on real images. Dice is a metric that measures how good a segmentation is, compared to manual segmentation by a doctor, with a maximum value of 1. For further details of the results, see (Akbar et al., 2024). This means that sharing synthetic medical images is a viable option to sharing real images, which can lead to the development of better segmentation networks. For this purpose, we have also investigated to which degree GANs and diffusion models memorize the training images, to avoid sharing real images from the training set. We found that diffusion models are more likely to memorize the training images (Akbar et al., 2023), and that researchers therefore should be careful when using diffusion models for sharing of synthetic medical images.

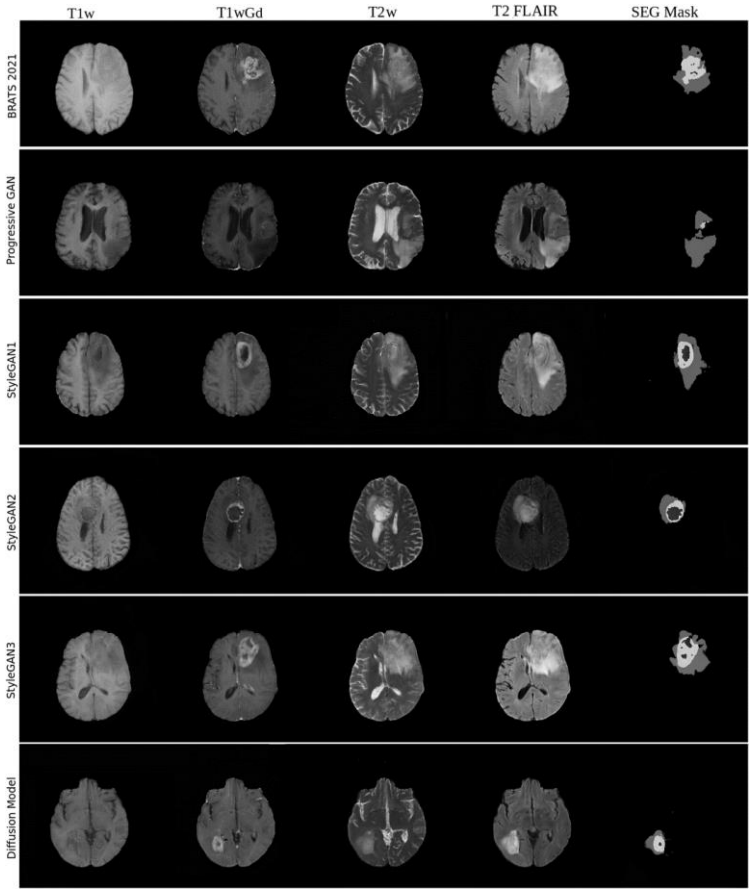

Figure 7 Synthetic 5-channel images obtained when training generative models using the open BraTS 2021 dataset. Each row shows a generative model, except for the top row which shows a real example, and each column shows a different MR sequence.

	Model	Orig	Aug	ET	ED	NCR/NET	Mean
U-Net	None	✓	✓	0.791 ± 0.009	0.785 ± 0.003	0.610 ± 0.008	0.729 ± 0.004
	Progressive GAN	✓	✓	0.790 ± 0.010	0.790 ± 0.007	0.609 ± 0.012	0.730 ± 0.008
	StyleGAN 1	✓	✓	0.769 ± 0.033	0.759 ± 0.047	0.593 ± 0.032	0.707 ± 0.037
	StyleGAN 2	✓	✓	**0.802 ± 0.009**	**0.794 ± 0.005**	**0.614 ± 0.009**	**0.737 ± 0.009**
	StyleGAN 3	✓	✓	0.769 ± 0.042	0.743 ± 0.060	0.582 ± 0.062	0.698 ± 0.054
	Diffusion	✓	✓	0.797 ± 0.020	0.785 ± 0.025	0.616 ± 0.014	0.733 ± 0.019
	None	✓		0.787 ± 0.010	0.783 ± 0.004	0.606 ± 0.009	0.726 ± 0.005
	Progressive GAN	✓		0.786 ± 0.010	0.784 ± 0.011	0.608 ± 0.010	0.726 ± 0.008
	StyleGAN 1	✓		0.783 ± 0.028	0.769 ± 0.035	0.602 ± 0.025	0.718 ± 0.029
	StyleGAN 2	✓		0.799 ± 0.013	0.788 ± 0.008	0.611 ± 0.011	0.732 ± 0.009
	StyleGAN 3	✓		0.777 ± 0.031	0.764 ± 0.047	0.599 ± 0.048	0.713 ± 0.041
	Diffusion	✓		0.794 ± 0.017	0.785 ± 0.017	0.613 ± 0.011	0.731 ± 0.014
	Progressive GAN		✓	0.668 ± 0.016	0.607 ± 0.048	0.468 ± 0.025	0.581 ± 0.026
	StyleGAN 1		✓	0.029 ± 0.017	0.167 ± 0.107	0.071 ± 0.036	0.089 ± 0.048
	StyleGAN 2		✓	0.750 ± 0.007	0.732 ± 0.013	0.553 ± 0.018	0.678 ± 0.009
	StyleGAN 3		✓	0.714 ± 0.021	0.709 ± 0.047	0.497 ± 0.057	0.640 ± 0.041
	Diffusion		✓	**0.791 ± 0.006**	**0.790 ± 0.005**	**0.610 ± 0.006**	**0.730 ± 0.004**
	Progressive GAN			0.546 ± 0.129	0.457 ± 0.159	0.360 ± 0.113	0.454 ± 0.130
	StyleGAN 1			0.022 ± 0.014	0.129 ± 0.099	0.057 ± 0.032	0.069 ± 0.044
	StyleGAN 2			0.562 ± 0.208	0.499 ± 0.238	0.376 ± 0.190	0.479 ± 0.206
	StyleGAN 3			0.682 ± 0.039	0.658 ± 0.067	0.444 ± 0.073	0.595 ± 0.059
	Diffusion			0.784 ± 0.009	0.783 ± 0.008	0.604 ± 0.008	0.723 ± 0.008

Figure 8. Obtained Dice scores when training a segmentation network with real (orig) and synthetic images, and testing on real images.

Federated learning for segmentation of tumour and organs at risk

For federated learning, we have demonstrated that it is possible to train a segmentation network (that segments the brain tumour as well as organs at risk) with data from different cities, without sending the data around, see Figure 7 for the main idea of federated learning.

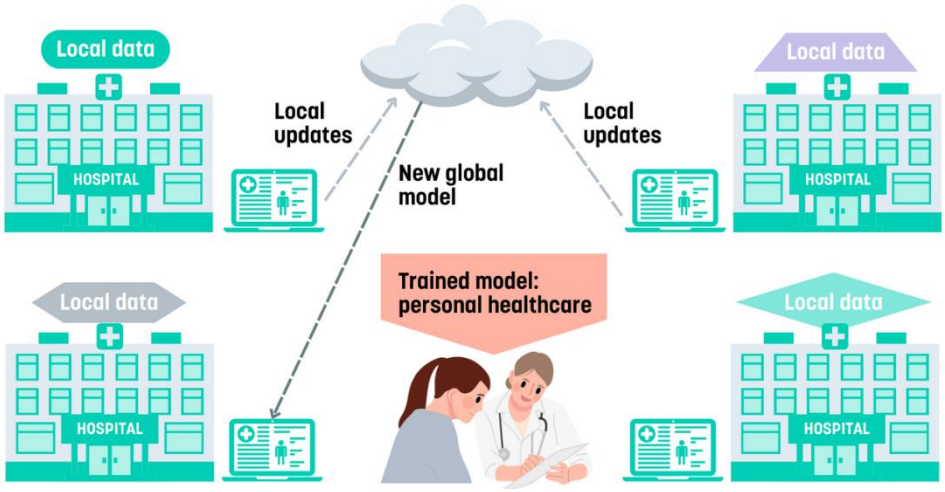

Figure 9. The main principle of federated learning. Instead of storing all data on one computer, a computer at each hospital stores the local data from that hospital. A global model is then trained through real-time communication of the model between each hospital and a combiner/global server (the cloud in this image), thereby using all the data.

The federated trainings were performed using the frameworks FEDn by Scaleout Systems (Ekmefjord et al. 2022) and iFusion by Inovia AI (based on Nvidia FLARE). A 3D U-Net was used, which takes four MR volumes as input (T1w, T1w contrast, T2w FLAIR, T2w contrast), see Figure 8, and returns segmentations of GTV, CTV and brain stem. Prior to federated trainings, data were preprocessed to result in volumes of 256 x 256 x 140 voxels, with 1 x 1 x 2 mm resolution. The trainings were performed using 25 subjects in Linköping (exported from Region Östergötland's oncology clinic's radiotherapy department), and 32 in Lund (exported from the radiation therapy clinic at Skåne University Hospital, about 400 km apart). 20% of the data were used for validation at each site.

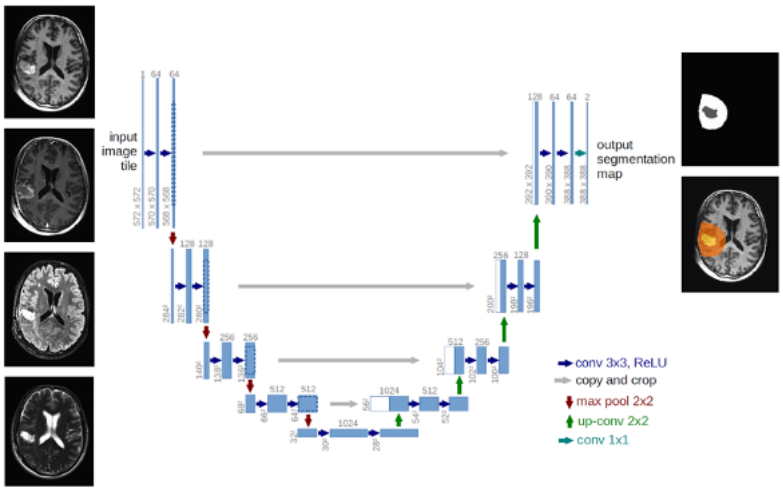

Figure 10. Federated segmentation of tumor and risk organs was performed using a U-Net, which takes several MR volumes (left) as input and returns segmentation maps (right). The U-Net travelled around Sweden during the federated trainings, while the data stayed at each hospital.

Table 1 shows the validation performance after federated trainings between Linköping and Lund, showing that the global (federated) model performs better than the local models. Trainings have also been performed with 3 Swedish cities (Linköping, Lund, Umeå University), and with 10 clients in a simulation.

	Lunds validation set	Linköpings validation set	Average score
Federated model best average	0.7419	0.8326	**0.7873**
Federated model best Lund	**0.7424**	0.8292	0.7858
Federate model best Linköping	0.7377	**0.8363**	0.7870
Local Lund	0.7402	0.8026	0.7714
Local Linköping	0.3524	0.8037	0.5781

Table 1. Comparison of local and federated models for segmentation (Dice scores), showing that the federated model performs better.

Federated learning for dose prediction

For federated learning, we have also demonstrated that it is possible to train a dose prediction network (that predicts the radiation dose to apply in every part of the brain, from all segmentations) with data from different sources, without sending the data around. The federated trainings were performed using the framework iFusion by Inovia AI (based on Nvidia FLARE). A 3D U-Net was used, provided by RaySearch, which takes nine binary segmentations as input (CTV, PTV, left optic nerve, right optic nerve, chiasm, brainstem, left eye, right eye, body outline) and returns the dose in each voxel (using a regression loss function). The setup is similar to Figure 8, but the inputs are instead the binary segmentations and the output is the dose volume (with values between 0 and 1). Prior to federated trainings, data were pre-processed to result in volumes of 75 x 75 x 75 voxels, with 3 x 3 x 3 mm resolution. The trainings were performed using 10 subjects in Linköping (exported from the radiotherapy clinic, as for segmentation), and 133 subjects from the open GLIS-RT dataset (Shusharina et al., 2021). 20% of the data were used for validation. Federated trainings will also be performed between Linköping and Lund with local data from each city.

Figures 9 – 10 show that the federated model results in a lower validation error compared to the local models. Training the dose prediction model with only GLIS-RT data resulted in a validation error of 0.84. Training with only Linköping data resulted in a validation error of 4.41, due to a much smaller dataset. The federated model resulted in a validation error of 0.77 and 2.00 respectively, thereby performing better for both sites.

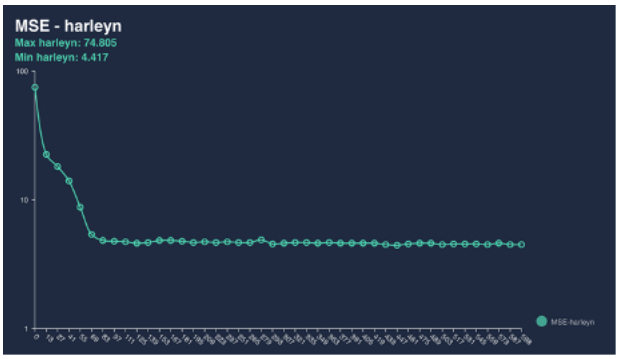

Figure 11. Training the dose prediction model with only Linköping data, resulting in a validation error of 4.41.

Figure 12. Training the dose prediction model through federated learning, resulting in validation errors of 0.77 and 2.00, which is smaller compared to the local models.

Integration of federated models in clinical software

To demonstrate that the models trained through federated learning can be used in clinical software, the federated segmentation model was integrated with Spectronic's SAINT (Spectronic Artificial INtelligence Technology) software system, which is a framework for transferring data between imaging modalities and applications that process the images. Figure 11 illustrates how DICOM images are sent from an MRI machine to the SAINT server, where the medical imaging app processes the data. The output from the app is then transmitted to a treatment planning system (TPS) for further processing.

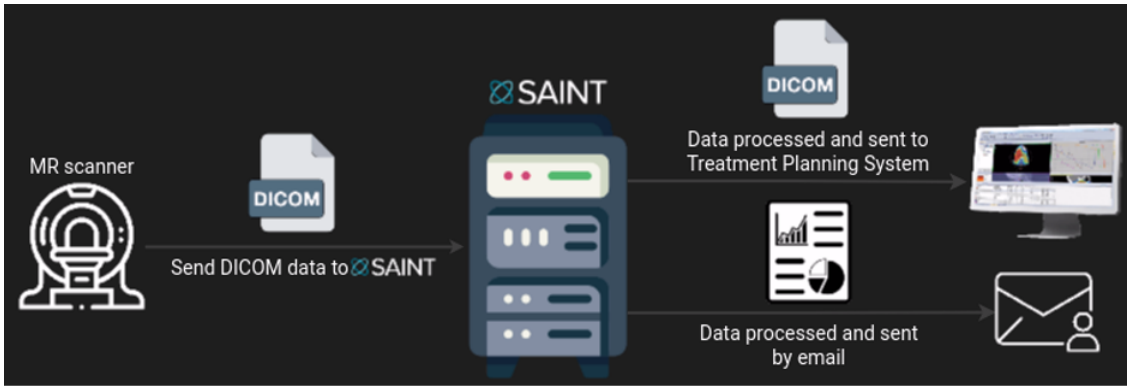

Figure 13. Schematic of the data flow to and from the SAINT software system.

With the final brain use case demonstrator we have shown that we can install a third-party application that runs a brain tumor segmentation algorithm on the SAINT software system. The app is downloaded and installed through a SAINT "app store" which is a web service that the SAINT server connects to. This service also allows new upgrades to be downloaded to the SAINT server in a clinical setting. In the demonstrator 1208 MRI images are sent over a network to SAINT, which receives the DICOM images and relays them to the segmentation app. The app generates an RTSTRUCT file (structures for radiotherapy) as seen in Figure 12. Finally, the SAINT software system takes the RTSTRUCT file and sends it to a TPS. Table 1 shows the execution time of the process. These segmentations are then used in RaySearch's RayStation software for dose prediction.

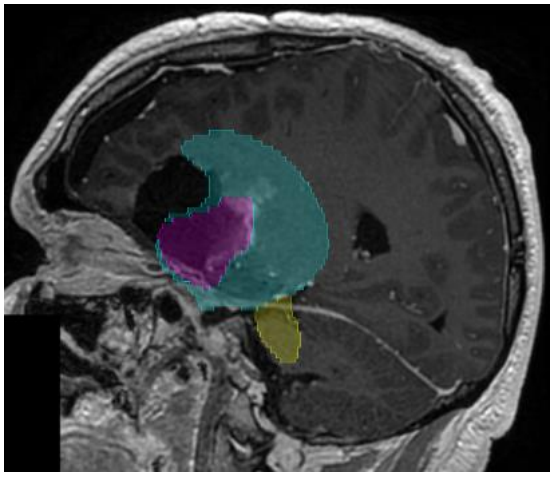

Figure 14. Generated RTSTRUCT overlaid on the original MR images.

	Time (s)
DICOM transmission	80
Image processing	190
Total execution time	**270**

Table 1. Execution times for the segmentation demonstrator.

Deep learning methods for diffusion MRI

We have developed advanced diffusion MRI methods that make use of MRI acquisitions featuring general gradient waveforms for investigating microstructural information not available via traditional methods. To this end, we introduced the methods called Q-space trajectory imaging with positivity constraints (QTI+) (Herberthson et al., 2021) and diffusivity-limited q-space trajectory imaging (QTI±) (Boito et al., 2023) demonstrating that enforcing relevant mathematical constraints during parameter estimation improves the estimates even when the number of diffusion-weighted volumes is small. The latter allows for shorter scan times making the technique suitable for clinical studies. However, constrained optimization requires computationally-intensive fitting routines leading to long computation times. Thus, we have explored the possibility of employing deep learning to speed up the QTI parameter estimation, while retaining strict positivity constraints. The developed neural network and the results obtained from a tumor patient (Boito and Özarslan, 2023) are illustrated in Figure XYZ. The results closely resemble those produced employing state-of-the-art routines, while providing smoother maps and about two orders of magnitude faster estimations.

In addition, we have focused on mapping the fiber orientation distribution function (fODF), which is employed in mapping the white matter fiber tracts through a procedure referred to as tractography. Having a wiring diagram of the brain allows us to identify the most important connections, which could aid in surgical planning. However, the MRI voxel size is orders of magnitudes larger than the diameter of axons which introduces significant challenges in obtaining reliable connectivity information. Thus, we developed and assessed a deep learning method for increasing the spatial resolution of the field

of fODFs. Our results exhibited superior recovery of information at high-resolution compared to traditional interpolation methods. The fODFs reconstructed were found to be more accurate than that can be obtained via high-resolution scans that suffer from low signal-to-noise ratio. In Figure PQR, we show the upsampled generalized anisotropy maps as well as exemplary tractography results obtained through our super-resolution method.

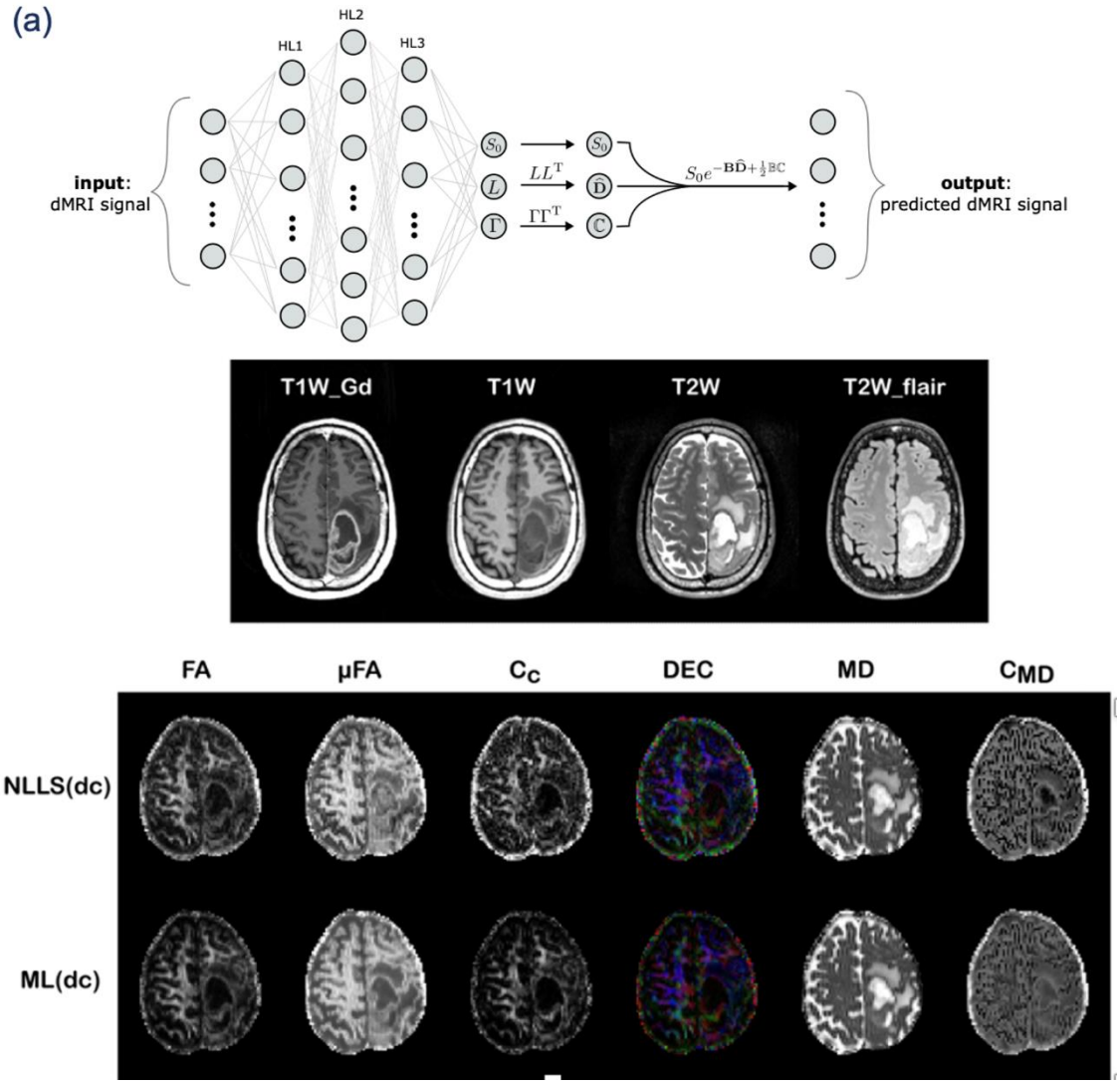

Fig. 15: (a) The neural network employed in training. A MultiLayer Perceptron (MLP) with three hidden layers is used to compress the input signal into the 28 parameters of the q-space trajectory imaging (QTI) model, from which the predicted dMRI signal is reconstructed to compute the loss.
(b) Results on one of the tumor datasets. The top row displays the standard clinical images including the Gd-enhanced T1-weighted map, T1-weighted image without contrast agent, T2-weighted image, and T2-weighted fluid attenuated inversion recovery maps. The bottom part shows the QTI-derived maps for the constrained nonlinear least squares (NLLS(dc)) method, followed by the constrained machine learning technique we developed (ML(dc) and ML*(dc)) in the last two rows.

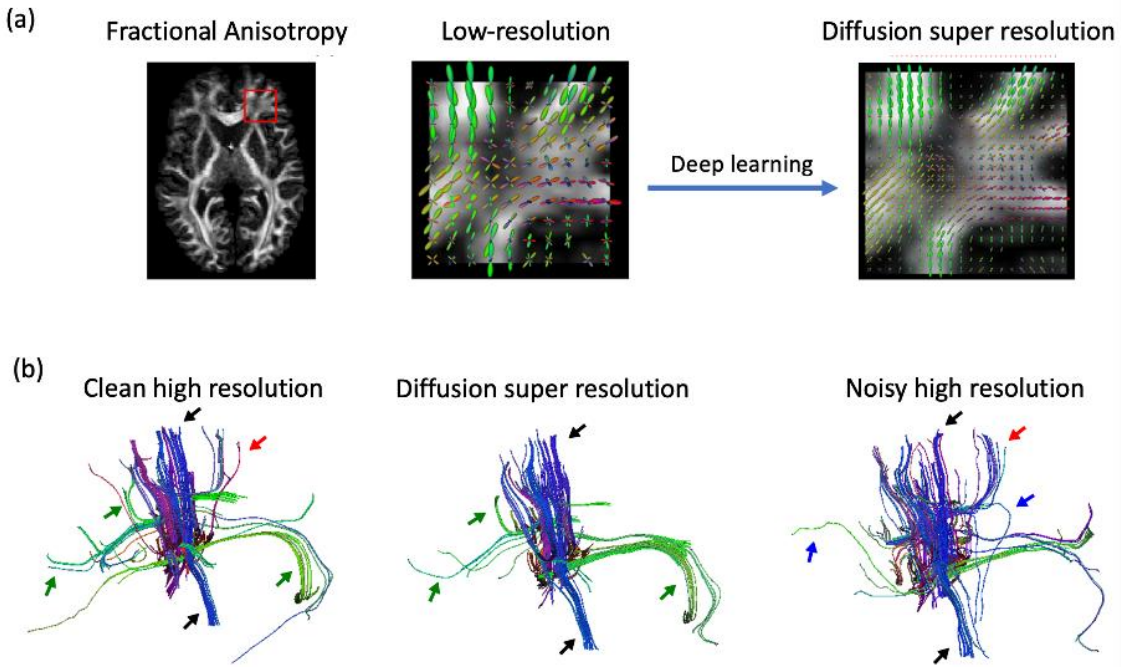

Figure 16: (a) The low-resolution and super-resolution fODF maps in a given ROI within a crossing fiber region obtained from the Human Connectome Project data. (b) Black arrows: correct tracts obtained from both methods. Green arrows: correct tracts obtained from DSR only. Red arrows: correct tracts obtained from high resolution acquisition only. Blue: false tracts obtained from only the high-resolution acquisition.

2.3 Lung Cancer

Owner: Philips – William van der Sterren

2.3.1 Introduction

Lung cancer is a common disease, with an incidence of 2.1M worldwide (2018). Worse, lung cancer is the leading cause of cancer death (18.4%, 1.7M, 2018 (IARC, 2018)). In addition to primary lung cancer, the lungs are also the second most frequent location of metastatic disease, with colorectal carcinoma, renal cell carcinoma and breast cancer most often metastasizing in the lungs (Society, 2019).

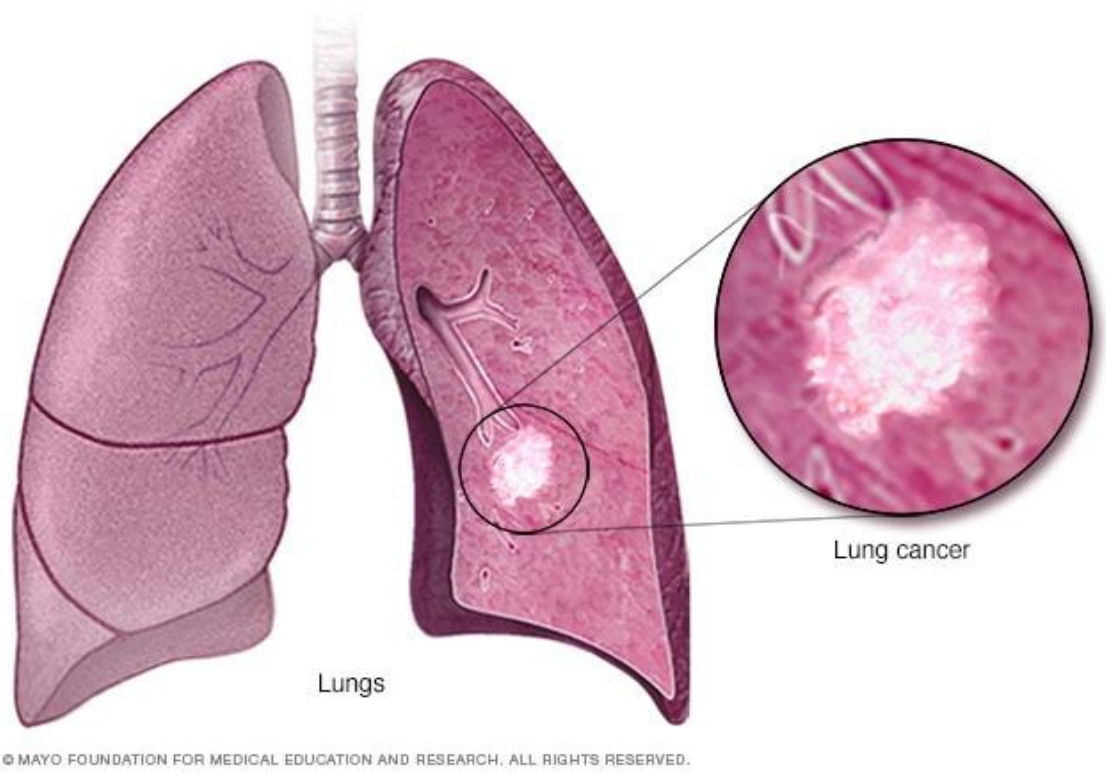

Figure 8 Lung cancer originates from the cells in the lungs (Mayo, 2022)

A common intervention for a suspicious lung nodule is a biopsy to determine, and if necessary, stage lung cancer; tissue is obtained from the lung nodule either via the airways (using a bronchoscope), percutaneously (using a needle) or surgically. In the USA in 2006, some 75,000 bronchoscopic lung biopsies were performed, and 12,000 surgical lung biopsies.

In case lung cancer is confirmed, and depending on the lung cancer progression (stage), therapy will either be focused on curing the patient, or on improving quality-of-life for the patient. Several treatments are available, including surgery, systemic (chemo) therapy, radiation treatment, thermal ablation and immunotherapy.
In general, there is a trend to more minimal invasive therapy.

2.3.2 Clinical state of the art

The journey of a lung cancer patient typically involves detection of symptoms / suspicious nodules, a biopsy procedure to confirm malignancy and stage the cancer, treatment planning, one or more treatments, and monitoring of the patient.

Patients may report with symptoms at their GP. Alternatively, patients may be invited to a lung screening because of their risk profile (heavy smoking, exposure to dust), and be flagged as having a suspicious lung nodule on a lung screening CT. In some cases, patients are flagged as having a suspicious nodule as an incidental finding on an ordinary thorax CT.

Typically, for a suspicious nodule larger than 10mm, a biopsy is planned to obtain tissue for pathology.

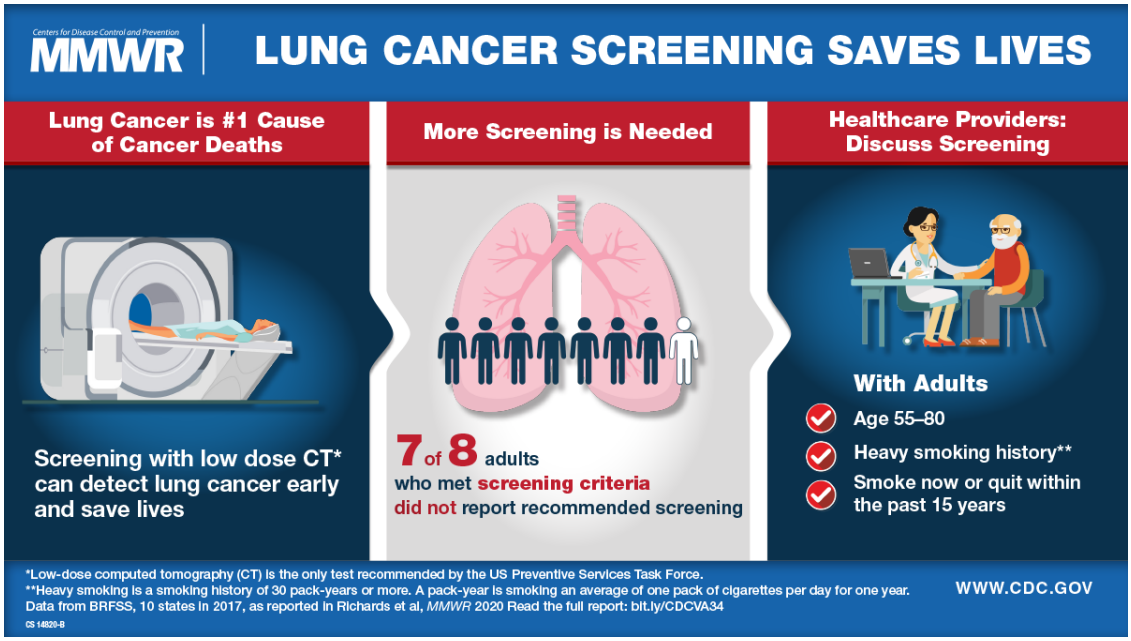

Figure 9 Poster informing the public about the benefits of lung cancer screening (Prevention, 2017)

Endobronchial biopsies are the preferred way to obtain tissue. It is challenging to reliably obtain samples from from lung nodules when these are peripheral and small (<20 mm), with diagnostic yield around 50% when solely using bronchoscope and 2D mobile C-arm. The alternative is to percutaneously obtain tissue using a long needle, guided by a CBCT or CT; this procedure has a higher risk of complications.
A low diagnostic yield from biopsies is problematic because of the uncertainty and discomfort for the patient, and because delays in treatment increase mortality (mortality increases with 1% / week).
Advanced endobronchial navigations systems (EBN), 3D CBCT imaging, and robotics are currently being adopted to increase diagnostic yield.
Also ‘rapid on-site evaluation’ (ROSE), an intra-procedural quick microscopic inspection of the tissue sample can improve diagnostic yield, by providing feedback to the pulmonologists that the sample was insufficient or taken from normal lung parenchyma instead of the suspicious nodule. This ROSE, however, cannot be used for diagnosis.

Figure 10 Endobronchial navigation assisted with 3D imaging

Figure 11 Endobronchial navigation assisted with robotics

After the biopsy, the sample tissue from the nodule, perhaps together with additional samples from the lymph nodes, are analysed by a pathologist. The pathology report is input for diagnosis and staging of the nodule.
The suspicious nodule might be diagnosed to be benign, for example, just an inflammation. Or it might be diagnosed as cancer. Lymph node samples help staging the nodule: the nodule might be small, isolated and early stage, corresponding to a good outlook for curative treatment. Or the nodule might be large, spread out also into the lymph nodes and late stage, in which curative treatment might not be realistic, but palliative treatment can help lengthen survival and improve quality of life.

Various treatments are available, including surgical resection, chemotherapy, radiation therapy, and thermal ablation, the latter two being less invasive.

Thoracic surgery or surgical resection will aim to take away that part of the lung containing the cancer nodule, including sufficient margin (which is healthy tissue immediately surrounding the nodule, more likely to also include cancer cells).
Surgical resection is becoming less invasive, transitioning from open surgery requiring lengthy recovery, towards key-hole surgery using an endoscope, with or without robotics. In addition, there is a trend to preserve more of the lung and resect less, going from resection of a complete left or right lung to resection of a single lung lobes and to solely resecting a single lung lobe segment, provided the nodule is nicely located in a single segment.

Thermal ablation of the nodule is an established procedure when performed using ablation needles by the interventional radiologists. One or more needles are introduced via the skin (percutaneous) in or near the cancer nodule. Next, ablation is performed for five to ten minutes, heating or freezing the tissue in the surroundings of the needle tips in order to damage the cancer cells. Over the next days and weeks, the cancer nodule disappears, leaving only scar tissue in the lung.
The downside of using needles for ablation is the occurrence of pneumothorax (a minor complication).
Device vendors currently are trialing variants of these ablation device in the shape of flexible catheters which can be introduced via the airways by the interventional pulmonologist. These devices create the ability to treat the lesion in the same procedure as the biopsy, reducing waiting time and stress for patients.

Treatment follow-up typically is done using 3D imaging, CT and/or PET. During follow-up, it is key to study the progression of the nodule, which ideally reduces in size.

Image processing is key to help the radiologist register and overlay images from multiple sessions in order to assess the progression.

2.3.3 Workflow inefficiencies and bottlenecks

The main workflow inefficiencies and bottlenecks consist of:

- The increasing inflow of lung screening scans and corresponding biopsies of small peripheral nodules, both increasing the number and complexity of biopsy procedures
- Moving towards 'less invasive treatment' for lung cancer, reducing recovery time, burden and support needs required for patients

In order to cope with increasing inflow of lung screening scans, radiologists need help processing and diagnosing more scans.
Image processing software and computer assisted diagnosis play an important role in processing more chest CTs, for screening or incidental, without massively increasing the workload for the radiologists who is to read the CT scans. Suspicious nodules can be flagged automatically, as can CT scans who lack suspicious nodules.

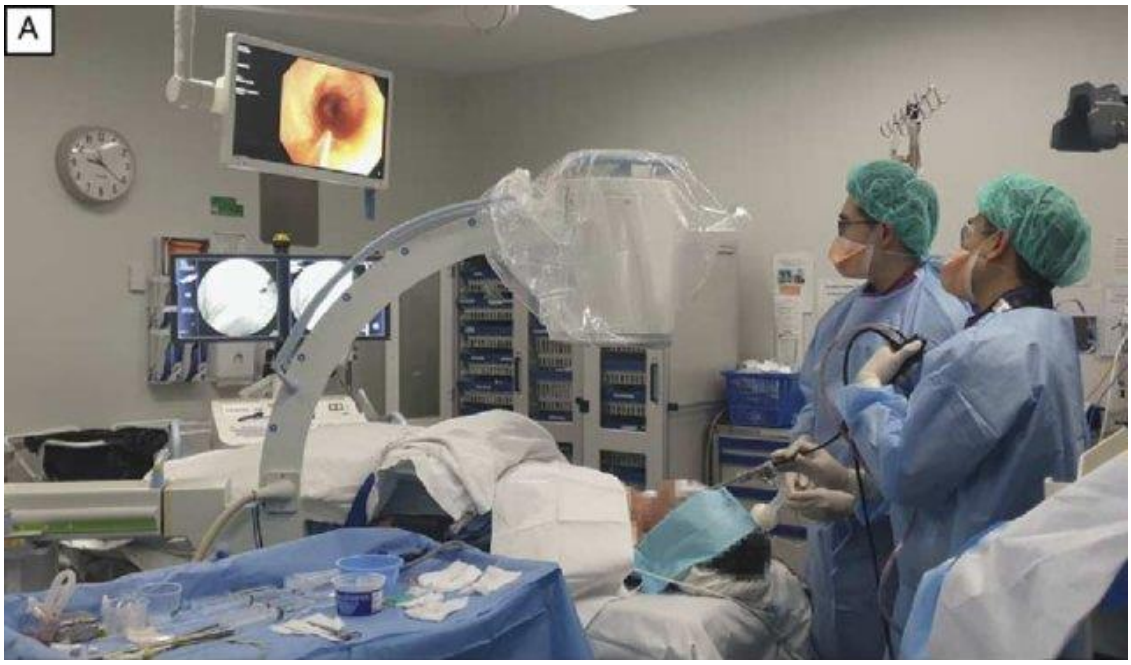

Figure 12 Traditional bronchoscopic lung biopsy with 2D fluoroscopy

To cope with the increasing number of smaller, more peripheral, biopsies, interventional pulmonologists need assistance to increase the diagnostic yield (the ability to obtain a diagnostic tissue sample) while reducing procedure time.

These smaller peripheral nodules are often not 'fluoro-visible' (that is, they cannot be seen in 2D fluoroscopy X-ray imaging), are beyond the reach and vision of the bronchoscope, and may be in parts of the lung which are hard to reach (upper segments) or in parts of the lung which move a lot with breathing (lower segments, just above the diaphragm).
Without additional means to see the lesion, the biopsy device, and their relative positions, pulmonologists struggle to successfully obtain tissue from the suspicious nodule.

Advanced endobronchial navigations systems (EBN) track the biopsy device, and provide real-time feedback on the device position during navigation, using a pre-operative CT scan as reference. Use of EBN alone is associated with a modest increase in DY (from 50% to 70%). However, EBN systems are unable to see the lesion, and suffer when the patient's lungs are deformed differently on the table during the biopsy than on the CT couch during pre-op CT imaging.

Three-dimensional cone-beam CT imaging systems are able to show the biopsy device and lesion and their relative positions in the lung. The lesion position may be overlaid on live fluoroscopy as a target (augmented fluoroscopy). Use of CBCT is associated with large increase in DY (to up to 90%).
The use of cone beam CT systems does present a significant learning curve for pulmonologists, though.

Endo-bronchial robotics support the pulmonologist with navigation and steerability, making it easier to navigate the catheter into hard-to-reach peripheral areas of the lung. Use of robotics alone is associated with a modest increase in DY (from 50% to 70%). Like EBN, robotics systems also are unable to see the lesion, and suffer from CT-to-body divergence.

In order to adopt 'less invasive treatments', more accurate anatomical information and planning and guidance software are required.
To enable these smaller resections, more accurate information about the lung (fissures, vasculature) needs to be made available during the surgery. This requires both improved (AI-based) segmentation algorithms to extract detailed anatomic information from pre-op images. And a translation of the anatomic information to patient on the table during the intervention, where the lung might be collapsed and flipped.

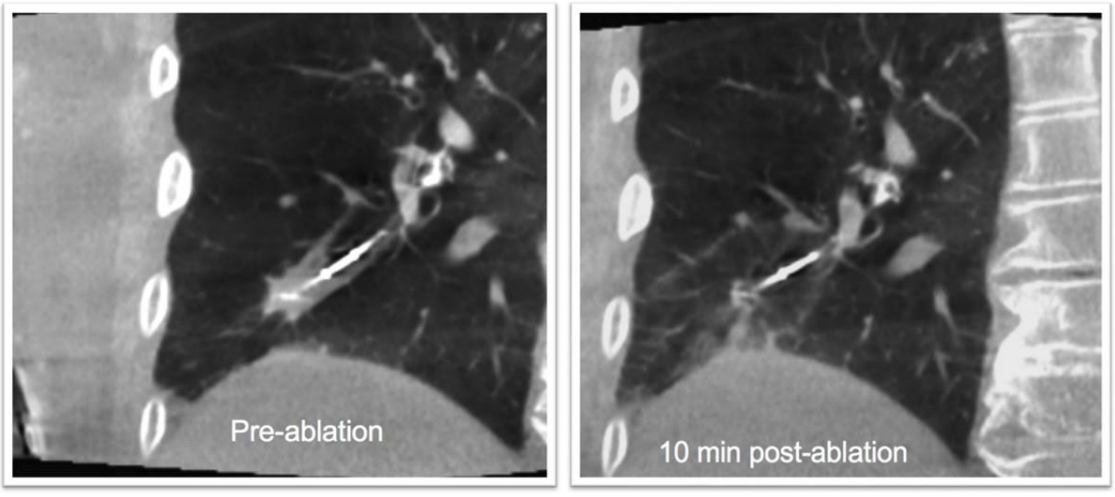

Figure 13 MW ablation via an endobronchial catheter (device in clinical trial)

To enable adoption of novel endobronchial ablation devices, interventional pulmonologist need planning and guidance software to help them identify the ablation positions offering sufficient coverage of the lesion and margin, both on pre-op CT and on in-op CBCT.

2.3.4 Outcomes and project results

The project has focused on improving the workflow and guidance in peripheral lung biopsies, and on improving automatic analysis of lung images in order to enable less-invasive treatments.

The improvements of the peripheral lung biopsy workflow have been realized in the form of a Philips investigational device which has been deployed and is being evaluated as part of a Philips sponsored clinical trial (still ongoing).

The improvements in automated analysis of the lung have been realized as a large part as new and improved functions as part of the LungQ 3.0 software, with CE and FDA clearance, announced May 2024.

The next sections provide more detail on both improvements.

Improvements of the peripheral lung biopsy workflow
Philips developed an investigational device of navigation software for lung biopsies. This investigational device was created for evaluation in a Philips sponsored clinical trial together with the RadboudUMC Nijmegen pulmonology team of prof. dr. Erik van der Heijden.

Early on in the design, the role of the pre-op CT scan and of a detailed airway tree extracted from the scan was identified. In cooperation with Thirona, Thirona's automatic airway segmentation algorithm was tuned for lung biopsy planning, and integrated in Philips navigation software.

In the clinical trial of the navigation software, an interim evaluation was performed after the first 13 procedures, identifying successful improvements as well as limitations:

- Successful features
    - Airway segmentation on CT, and availability of the airway tree when navigating on CBCT
    - Catheter detection
    - Low dose confirmation scans
- Limitations
    - Mismatch between actual tasks and task structure in the navigation software
    - CT- CBCT registration

The second iteration of the investigational device has been developed to address the limitations.
In the paragraphs below, we explain the improvements realized in by comparing the prior imaging workflow in these lung biopsy procedures, and the new imaging workflow as enabled by the investigational device.

Improvements of the peripheral lung biopsy workflow – prior workflow
The prior workflow for lung biopsies had already adopted 3D intra-procedural imaging for 'tool-in-lesion' confirmation, but heavily relied on manual inspection and interpretation of 3D scans to plan navigation and of mental mapping of that navigation information.

This is illustrated in Figure 14: ahead to the biopsy procedure, the interventional pulmonologist inspects the most recent high resolution CT volume, 'manually' scanning for airway paths that are near and leading towards the nodule. The pulmonologist memorizes the turns to make with a bronchoscope and biopsy catheter to arrive near the nodule.
Early in the biopsy procedure, the interventional pulmonologist acquires a CBCT volume of the patient. This volume will clearly depict the target nodule to be biopsied, and the pulmonologist will mark this target. After marking the target, this target can be projected on top of the live fluoroscopy images for all C-arm angles.
The interventional pulmonologist will navigate the bronchoscope and catheter near the nodule using fluoroscopy with the nodule being displayed on the overlay, mentally combining this with the memorized airway tree and navigation plan. To either confirm that the catheter is in the nodule, or to determine adjustments (moving the catheter forward, backward, or into another airway), an CBCT volumes is acquired and inspected. Any navigation corrections resulting from that inspection are again memorized and used to bring the biopsy catheter closer to the target nodule.
This navigation is both time consuming and more error prone because the airways are not visible on X-ray fluoroscopy.
Finally, when the catheter is in the nodule, biopsies are performed under fluoroscopy.

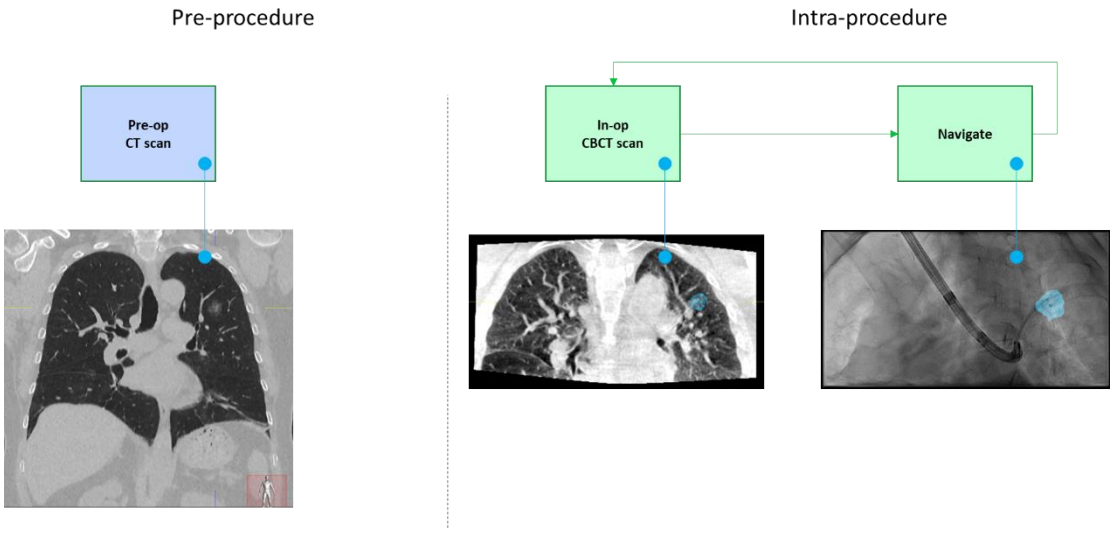

Figure 14 Illustration of the prior imaging workflow for peripheral lung biopsy

Improvements of the peripheral lung biopsy workflow – current workflow
In the proposed current workflow, as being evaluated in the clinical trial, the pre-procedural CT scan is analysed to segment the airway tree, by means of Thirona's airway segmentation algorithm. As soon as the interventional pulmonologist indicates the target nodule, the planning software will propose paths through the segmented airway trees that run close and towards the target lesion. This provides the interventional pulmonologist a visualization of potential airway paths to the nodule, and fly-through virtual bronchoscopy views to prepare for the procedure. The ability to prepare the procedure in the physician's office instead of in the exam room enables more efficient use of the exam room.

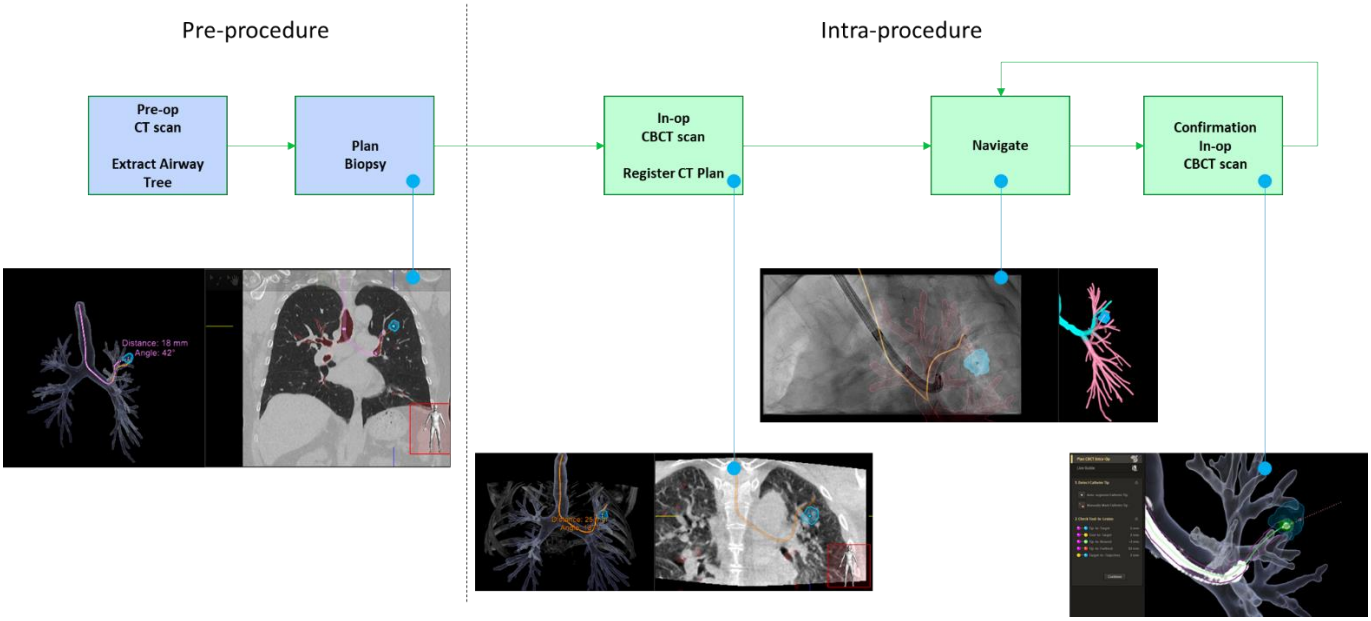

Early in the procedure, a 3D CBCT scan is acquired. The planning software supports registration of the pre-op CT scan to the CBCT scan, such that the nodule, airway tree and chosen paths are transferred to the CBCT scan. This information is now available for viewing, editing and for overlay on X-ray fluoroscopy, assisting the interventional pulmonologist with navigation, where now the chosen path through the airway tree and bifurcations along this path are being shown as an overlay on X-ray fluoroscopy. The planning software also supports the pulmonologist with confirmation scans in two ways:

- Biopsy catheters are detected, and the tip to nodule distance is indicated automatically, reducing the need for the pulmonologist to perform manual image analysis and 3D measurements;
- Low dose 3D confirmation acquisitions that reduce X-ray dose by being tuned to just highlight the biopsy device, with the lesion being registered from the prior normal dose CBCT scan. The aim is to lower the threshold to acquire 3D confirmation scans, as these scans clearly answer whether the tool is in the lesion.

Together, these improvements aid the interventional pulmonologist in successfully taking biopsies of the challenging small peripheral nodules, and make these procedures accessible to a larger group of interventional pulmonologists.

Improvements of the peripheral lung biopsy workflow – airway tree segmentation

Philips cooperated with Thirona to incorporate Thirona's airway tree segmentation algorithm in Philips planning and navigation software for interventional pulmonology procedures. Thirona tuned their airway tree segmentation algorithm towards the specific needs of endobronchial biopsy procedures, where airway tree bifurcations are more important than airway segment length.

During the midpoint evaluation in the clinical trial, the performance of the airway tree segmentation was rated as follows:

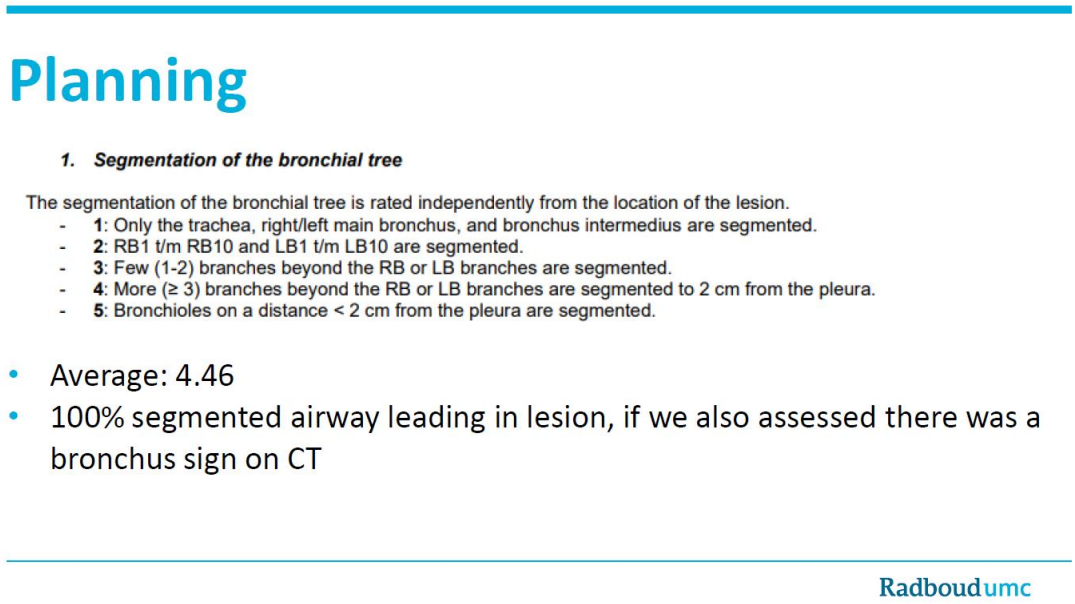

Figure 15 Performance of the airway segmentation on CT scans was found to always identify airways into the nodule (if there was one), to and to segment the smallest airways within 2cm of the pleura in nearly 50% of the cases.

Improvements of the peripheral lung biopsy workflow – catheter detection
The Philips planner's ability to segment the biopsy catheter proved popular, as it enables automatic 3D distance measurements towards the nodule, and serves are reference point of the prior catheter position on the overlay during X-ray fluoroscopy. The pulmonologist often took the effort to insert an X-ray opaque biopsy tool in the X-ray transparent hollow Medtronic Edge catheter with the purpose of enabling automatic segmentation.

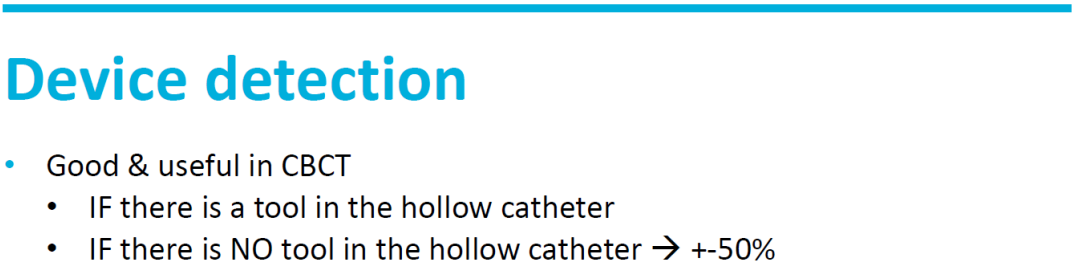

Figure 16 Feedback on biopsy catheter detection

Improvements of the peripheral lung biopsy workflow – low dose confirmation scans
Philips implemented novel type of low dose 3D confirmation scans where dose is reduced such that solely the biopsy catheter and major anatomical structures remain visible. When combined with a prior normal dose CBCT, 3D confirmation is facilitated at a fraction of the patient dose of a normal CBCT.

These low dose 3D confirmation scans did lead to the same decision (to reposition the catheter or to start biopsies) as a normal CBCT with the exception of very faint suspicious nodules (‘ground glass opacity’ (GGO) nodules).

The potential reduction in patient dose amounts to 39%.

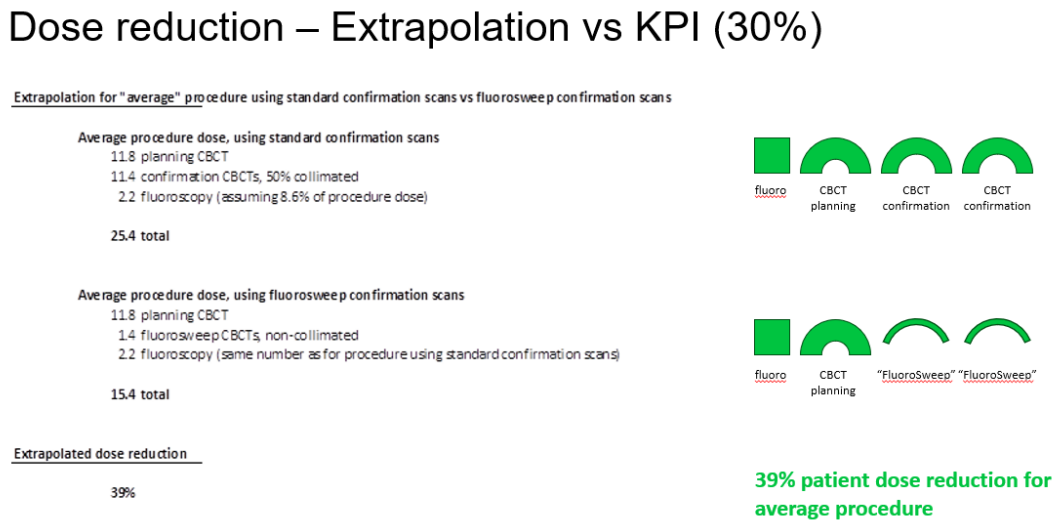

Figure 17 Extrapolated patient dose reduction when using the low dose (‘FluoroSweep’) confirmation scans instead of normal, 50% collimated, CBCTs

The improvements described above assist in dealing with an increase in peripheral biopsies, by making the required technology and data more accessible to the interventional pulmonologist.

Improvements in automated analysis of the lung

Automatic and advanced lung image analysis is key for current and future bronchoscopic and surgical applications. A successful bronchoscopic peripheral lung biopsy or treatment procedure relies on robust hardware and software components. This enables treating physicians to access crucial information and reduce the cognitive load of 2D to 3D translation. For bronchoscopic interventions, Thirona mainly focused on AI-based *airway segmentation* and *vascular segmentation* algorithms.

In addition, after malignancy confirmation by biopsy, resection of the cancerous tissue is a surgical intervention for treating lung cancer. Segmentectomy is becoming an important surgical option for treating early-stage lung cancer. It removes the cancerous lung segment while preserving more healthy lung tissue compared to a lobectomy. Planning of a segmentectomy requires advanced anatomical information as compared to traditional surgical options. For this application, Thirona mainly focused on the identification of the anatomical *segmental airway and parenchymal boundaries*; and the identification of the *pulmonary arteries and veins*. Because of the high patient-to-patient anatomical variability, AI-based algorithms are a crucial component for successful planning of the procedure

Improved made to the algorithms have been included as part of the Thirona’s LungQ 3.0.0 software release, which was CE and FDA cleared.

The performance of the following innovations were improved:

Improvements in airway segmentation and segmental airway labeling
A reliable and robust airways segmentation is a basis for many procedures. The algorithm needs to be highly specific while keeping a good sensitivity. The performance of the automatic airway segmentation in LungQ 3.0.0 was further improved compared to prior version of LungQ. The improvements successfully outperformed the prior version, both in sensitivity in peripheral regions as in robustness in difficult cases. (Note that the an earlier improved version was used in the Philips investigational device described above.) Segmental airway labelling additional helps to lower cognitive load as it provide anatomical meaning to an otherwise binary airway tree. Using advanced AI-based technology, the target of >90% accuracy was achieved and deployed in LungQ v3.0.0. The algorithm showed to have a very high accuracy in normal cases (e.g. with complete anatomical airways and little anatomical airway variation), but also showed high performance in more difficult cases e.g. with lobectomy or abnormal airway anatomy.

Improvements in automatic pulmonary segment segmentation
Identification of the pulmonary segmental boundaries is a difficult challenge since, opposite to the lobar boundaries, no physical boundary is visible on CT. Nevertheless, identification of this segmental border is a key driver to decide whether a surgical resection can be limited to a less invasive and lung sparing single segment resection. An automated segment segmentation algorithm was successfully developed and deployed in LungQ version 3.0.0, showing a performance close to the human reference.

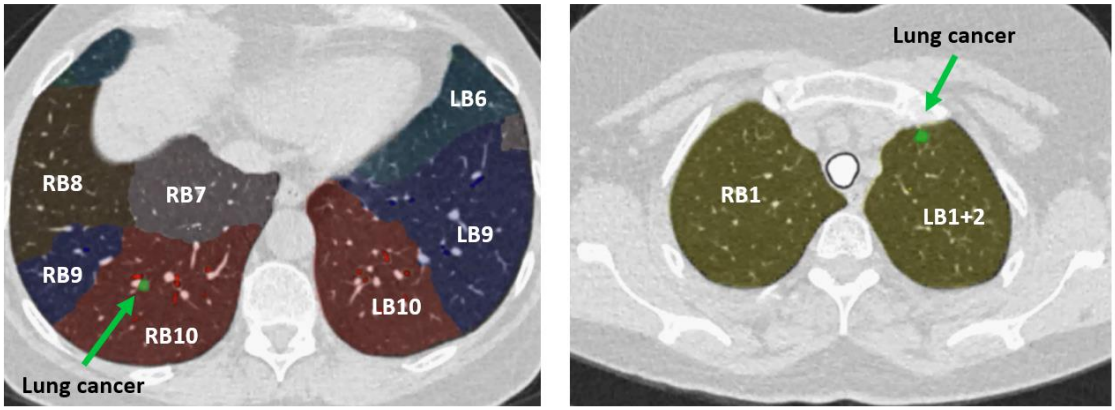

Figure 18 Automatically segmented pulmonary Segments (in color) in relation to malignant lesion.

Improvements in automatic Pulmonary artery and vein segmentation
Segmentation of the pulmonary vessel tree in arteries and veins has a range of applications. The current focus is on assisting trans-parenchymal path generation during bronchoscopic interventions and supporting surgical segmentectomy.

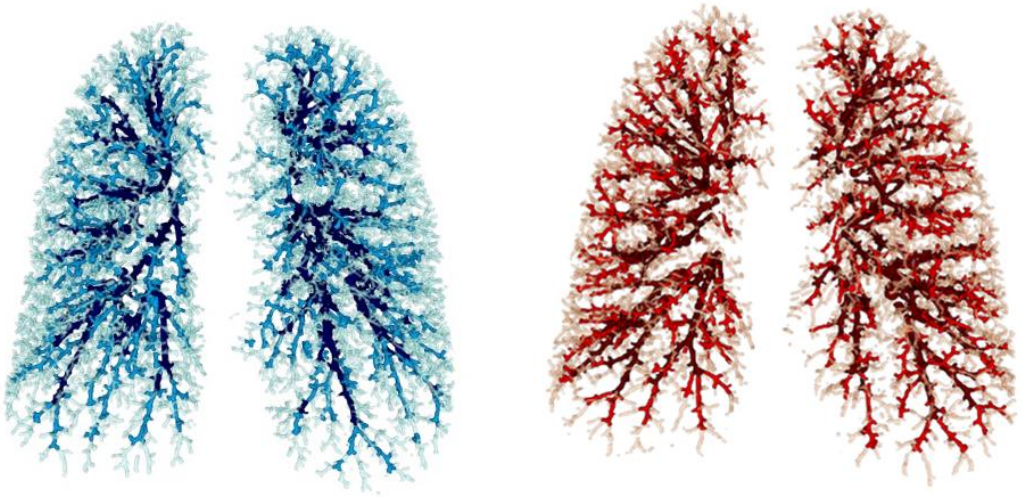

Figure 19 Segmentation of the pulmonary vessel tree in arteries (blue) and veins (red)

Algorithm improvements in the segmentation of pulmonary arteries and veins have resulted in crisper segmentations, fewer artery-vein false positives, and less over-segmentation of the vessel tree. These updates were deployed in LungQ v3.0.0.

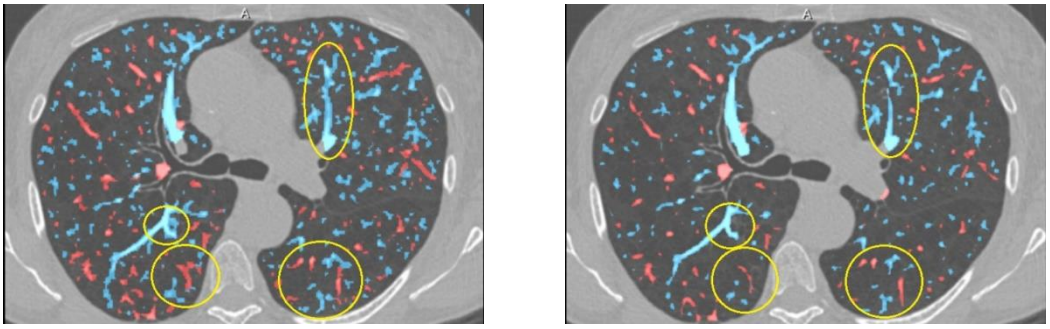

v1.0.0 **v2.0.0**

Figure 20 Improvements in algorithm v2.0 (LungQ v3.0.0) for the segmentation of pulmonary arteries and veins: crisper segmentations, fewer artery-vein false positives, and less over-segmentation

In summary, Thirona realized:

- High performing automatic airway segmentation and segmental airway labeling
- High performing automatic segmentation of the pulmonary segmental boundaries
- High performing automatic pulmonary artery-vein segmentation

The availability of more accurate analysis of lung CT scans as achieved by Thirona aids in adoption of less invasive treatments.

2.4 Hepato Pancreato Billiary oncology (HPB)

Owner: LUMC – Jouke Dijkstra

2.4.1 Introduction

Pancreatic cancer is 4th leading cause of cancer death in the United States. Prognosis is very poor with median survival of < 6 month in advanced cases. Upon diagnosis, the disease is associated with a 5-year survival rate ~10%. Surgical resection is the only curative option with an associated 5-year survival rate of up to 20-30% depending on the tumor size. However, discriminating between malignant and benign tissue can be challenging, especially after neoadjuvant treatment due to therapy induced fibrosis (TIF). In the same anatomical region cholangiocarcinomas arising from the epithelial lining of the biliary tree, are more rarely seen, they account for around 2% of all malignancies. They belong to a cluster of highly heterogeneous biliary malignant tumors that can arise at any point of the biliary tree. Cholangiocarcinomas are categorized according to anatomical location as intrahepatic (iCCA), perihilar (pCCA), or distal (dCCA). pCCA and dCCA can also be collectively referred to as 'extrahepatic' (eCCA). Prognosis, like in pancreatic cancer is very poor, due to silent presentation with advanced disease. Median survival was 10 months unrelated of stage of disease and with a 1-year and 5-year survival rate of 46% and 11%, respectively. As well as in pancreatic cancer complete surgical resection is the only possible curative option. Hence, the related anatomical location and morphological composition of extrahepatic cholangiocarcinomas (eCCA) and pancreatic (head) cancer, this is an interesting field of research for fluoresce guided surgery with tumor targeted fluorophores.
Currently, enhancing contrast of structures using near-infrared (NIR) fluorescence is a technique under development. It can provide accurate and real-time visualization of tumors during surgery. Fluorescent agents are intravenously administered and specifically bind to malignant cells or tumor-associated tissue, such as neoangiogenic vessels or stroma, and emit light in the invisible, near-infrared spectrum (i.e. 700-900 nm). Using a dedicated fluorescence imaging system, contrast of tumors relative to their background can be improved, which allows real-time image-guided surgery and improve complete resection rates. cRGD-ZW800-1 is a fluorescent contrast agent that specifically binds to integrins associated with neo-angiogenesis. It is a cyclic pentapeptide (cRGD) conjugated to the 800 nm NIR fluorophore ZW800-1. The cyclic 3-amino acid sequence (RGD) is clinically a well-known peptide that binds to various integrins (αvβ1, αVβ3, αvβ5, αvβ6, αvβ8, α5β1, α8β1 and αIIbβ3), mostly associated with neo-angiogenesis. Tumors larger than 1-2 mm depend on the formation of new blood vessels to acquire sufficient amounts of oxygen and nutrients. Some of these integrins are overexpressed on malignant cells and in tumor stroma, such as in breast, colorectal, pancreas and lung cancer. cRGD-ZW800-1 has successfully been used in colorectal cancer patients, identifying colorectal cancer during oncologic resection. Other RGD based molecules have been investigated in various phase I and phase II imaging studies using PET and SPECT and in a phase III study as an anticancer therapy (cilengitide). Recently, our group has initiated a phase II clinical trial investigating the application of a cRGD targeted PET tracer (18F-Fluciclatide) in the response monitoring of pancreatic cancer.

Estimated New Cases

	Males			Females	
Prostate	248,530	26%		Breast	281,550	30%
Lung & bronchus	119,100	12%		Lung & bronchus	116,660	13%
Colon & rectum	79,520	8%		Colon & rectum	69,980	8%
Urinary bladder	64,280	7%		Uterine corpus	66,570	7%
Melanoma of the skin	62,260	6%		Melanoma of the skin	43,850	5%
Kidney & renal pelvis	48,780	5%		Non-Hodgkin lymphoma	35,930	4%
Non-Hodgkin lymphoma	45,630	5%		Thyroid	32,130	3%
Oral cavity & pharynx	38,800	4%		Pancreas	28,480	3%
Leukemia	35,530	4%		Kidney & renal pelvis	27,300	3%
Pancreas	31,950	3%		Leukemia	25,560	3%
All Sites	**970,250**	**100%**		**All Sites**	**927,910**	**100%**

Estimated Deaths

	Males			Females	
Lung & bronchus	69,410	22%		Lung & bronchus	62,470	22%
Prostate	34,130	11%		Breast	43,600	15%
Colon & rectum	28,520	9%		Colon & rectum	24,460	8%
Pancreas	25,270	8%		Pancreas	22,950	8%
Liver & intrahepatic bile duct	20,300	6%		Ovary	22,950	5%
Leukemia	13,900	4%		Uterine corpus	12,940	4%
Esophagus	12,410	4%		Liver & intrahepatic bile duct	9,930	3%
Urinary bladder	12,260	4%		Leukemia	9,760	3%
Non-Hodgkin lymphoma	12,170	4%		Non-Hodgkin lymphoma	8,550	3%
Brain & other nervous system	10,500	3%		Brain & other nervous system	8,100	3%
All Sites	**319,420**	**100%**		**All Sites**	**289,150**	**100%**

Figure 21 (Siegel, 2021)

2.4.2 Clinical state of the art

The diagnostic workup for PDAC typically consists of a combination of CT for staging and endoscopic ultrasound with fine needle aspiration (EUS-FNA) or biopsy or endoscopic retrograde cholangiopancreatography (ERCP) to obtain histological confirmation of disease. Recently, magnetic resonance imaging (MRI) has gained ground for the primary evaluation of local disease stage and vascular encasement by tumor tissue, as well as the characterization of distant metastases, especially in the peritoneal cavity and liver. The role of 18F-FDG positron emission tomography (PET) combined with computed tomography (PET/CT) in the workup of pancreatic cancer remains controversial. The National Comprehensive Cancer Network (NCCN) consensus guideline states that FDG-PET/CT may be used per institutional preference; although, it is not a substitute for high-quality contrast-enhanced CT (ce-CT). The European Society for Medical Oncology (ESMO) states likewise and says the role of PET/CT should be further clarified. The individual treatment plan is based on various clinical and radiological parameters, including tumor stage, the presence of metastatic disease, the extent of tumor invasion into major blood vessels, and the patient's physical condition.
Determination of resectability of a pancreatic tumor with clear surgical margins is crucial, as only complete surgical resection of the tumor can provide curative-intent treatment. Constantly developing surgical techniques (e.g., robot-assisted surgery)

and the clinical introduction of (neo)adjuvant therapy have significantly improved patient outcomes in the past decade, resulting in a 30–40% five-year OS after complete (R0) tumor resection, compared to 17.4% in 2011. The incomplete surgical resection rates (R1 or up) vary enormously in the available literature, between 20 and 70% of all pancreatic resections for malignant disease show positive surgical margins, which dramatically increase the rate of local and early recurrence of pancreatic cancer. Aiming to increase the number of patients eligible for curative-intent resection and to further optimize surgical outcome, the combination of neoadjuvant induction therapy and adjuvant treatment has been under clinical investigation in the past years. There are currently two combinations recommended as first-line (neo)adjuvant treatment regimens by the NCCN and ESMO: (modified) FOLFIRINOX (Folic acid, 5-Fluoruracil, Irinotecan, and Oxaliplatin) or gemcitabine plus nab-paclitaxel, the last is often combined with radiation therapy. Since individual patient health status and morbidity highly influence the ability to receive (neo)adjuvant treatment, most well-considered multidisciplinary recommendations for duration and intensity of treatment are made within these standardized regimens or ongoing clinical trials for individual patients.

Focusing on neoadjuvant therapy (NT), the most clinical benefit could be gained within the borderline resectable and locally advanced patients; however, a standardized role in primary resectable disease should also be considered. NT aims to slow disease progression, decrease tumor volume and local extensiveness, as well as eradication of potentially ‘occult’ micrometastases. NT, on one side, provides an extended time-window to detect rapid progressive disease, thereby potentially avoiding futile surgeries. On the other side, it provides a way to increase the eligibility for curative-intent resection, raise the percentage of radical resections (R0) and improve the surgical outcome. The advantages of NT are underlined by the results of the recently published PREOPANC-1 trial. This trial compared clinical outcome and survival data of postoperative patients with resectable and borderline resectable disease who had received neoadjuvant or adjuvant therapy. Results showed improved survival and higher complete surgical resection (R0) rates in the neoadjuvant therapy arm, with a 30% increase in R0 resections (71% vs. 40%) and a 2-month prolonged median survival (16 vs. 14 months) [18]. More recently, the recruitment of patients for its successor, the PREOPANC-II trial (NTR7292) was completed. In this trial neoadjuvant treatment with FOLFIRINOX was compared to neoadjuvant Gemcitabine-Radiotherapy followed by adjuvant Gemcitabine in patients with (borderline) resectable disease.

To date, accurate assessment of response to (neo)adjuvant treatment remains challenging, which is a crucial step in re-staging and determination of resectability. Currently, treatment response is monitored with CT-imaging, which is evaluated by radiologists using the internationally standardized RECIST 1.1 criteria. These criteria focus on a percentual change in tumor dimensions (longest diameter), which are used to determine therapy response: a complete response (CR), partial response (PR), progressive disease (PD), or stable disease (SD). Although the role of this approach for assessment of response is limited, besides overestimation of tumor size on CT, the change in tumor attenuation is of limited value in the prediction of resectability, due to the inability to differentiate treatment-related necrosis, therapy-induced fibrosis (TIF), and tumor-associated pancreatitis (TAP) from residual vital tumor tissue in the pancreas. Cassinotto et al. concluded ce-CT lacks the sensitivity and performance for accurately monitoring treatment response, showing that the diagnostic performance of ce-CT to predict resectability decreased after neoadjuvant treatment (58% vs. 83%). Ferrone et al. showed similar results, stating that ce-CT after FOLFIRINOX treatment no longer adequately predicts resectability of the tumor. These results underline the

need for improved imaging methods for assessment of therapy response, since this is pivotal for accurate (re)staging and determination of tumor resectability. In addition to conventional CT-imaging, molecular-based FDG-PET/CT-imaging has been evaluated for monitoring of (neo)adjuvant treatment response in various malignancies, including PDAC. Despite some favorable results, the main disadvantage of FDG-based PET/CT-imaging of pancreatic tissue is the increased uptake seen in TAP, complicating adequate differentiation between the remaining tumor and adjacent benign tissue. Molecular-targeted tumor imaging has the potential to overcome these challenges by selectively targeting tumor biomarkers overexpressed on or in close proximity to PDAC cells, resulting in high tumor-specific signals with minimal background accumulation in surrounding normal tissue.
Following induction treatment and restaging, the next vital steps for curative intent resection are: intraoperative visualization and delineation of the tumor to its anatomical demarcations and relations with vital structures, identification of suspect tumor-containing lymph nodes, as well as assessment of the surgical margins for residual vital tumor. However, the complex and heterogeneous tumor characteristics of PDAC with its extensive desmoplastic reaction and locoregional changes resulting from NT as well as its retroperitoneally anatomical location make this very challenging. Near-infrared fluorescence (NIRF) imaging, also called fluorescence-guided surgery (FGS), a novel technique, can offer a solution by providing real-time intraoperative guidance by enhancing visual contrast for localization of the tumor and discrimination between malignant and benign tissue. FGS uses a fluorescent dye conjugated to a molecular tracer designed to bind specific molecular features on (tumor)-target cells (i.e., tumor tissue, tumor stroma, etc.). Aiding a surgeon with a tool that enhances intraoperative surgical navigation to detect tumor, lymph node, and metastatic deposits in real-time, might eventually result in fewer incomplete surgical resections (R1) and improve surgical outcome and OS in the near future.
Multiple molecular targets, or biomarkers, expressed by PDAC, have been identified in previous studies. These biomarkers form the basis for tumor-targeted nuclear and fluorescence imaging in various malignancies, including PDAC. Molecular imaging of oncological targets has been of particular interest in the past decade: multiple (pre)clinical trials have shown promising results for PDAC-targeted PET/CT and NIR-imaging, for diagnostic as well as therapeutic purposes.

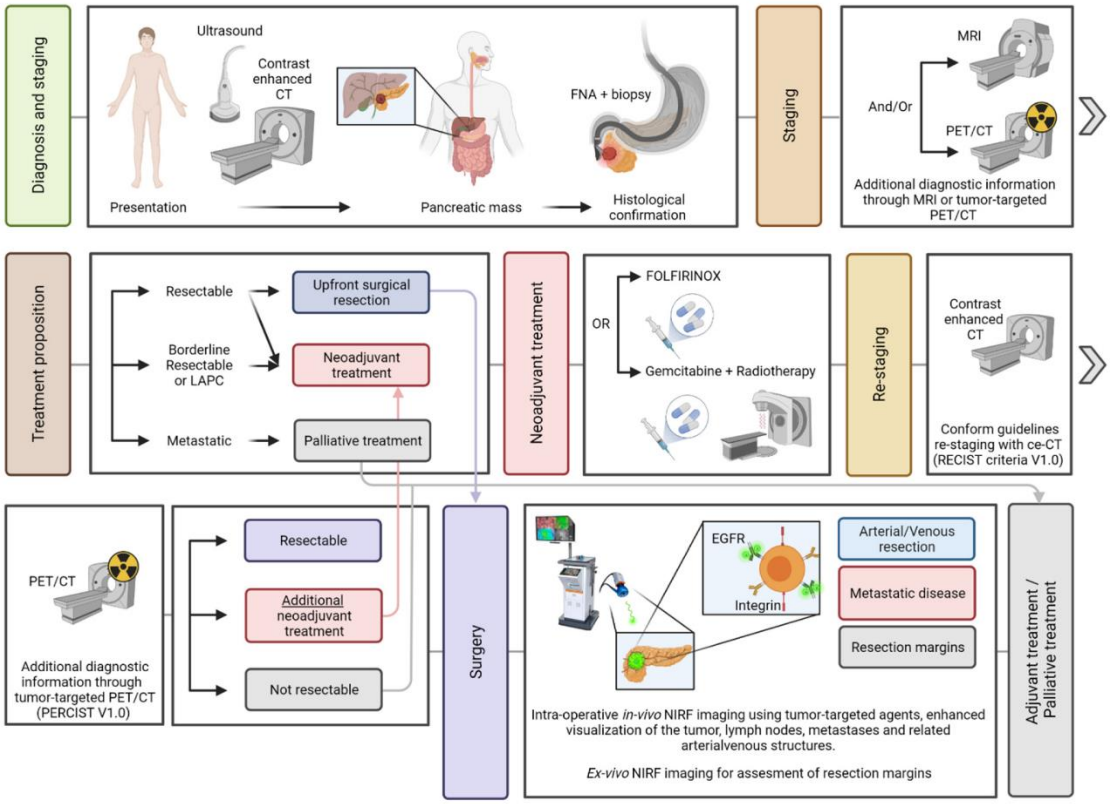

Figure 22 (van Dam, 2021)

2.4.3 Workflow inefficiencies and bottlenecks

- Quality of the scans for tumor delineation:
  - As described previously both CT and MR imaging have limited value in assessing vascular involvement. Therefore patients are incorrectly deemed irresectable;
- Accuracy of assessment of distant and nodal metastases for treatment planning:
  - MR imaging is more sensitive for the detection of liver metastases, however, CT imaging has shown to be superior to MR imaging in the detection of nodal metastases;
- The complexity of correct restaging after neoadjuvant chemotherapy which is important for selection of optimal treatment option:
  - Differentiation between fibrosis and malignant tissue is challenging after neoadjuvant chemotherapy;
- Interpretation of 2-dimensional scans remains challenging, especially in determining the circular involvement of the vital blood vessels surrounding the pancreas, i.e. mesenteric superior vein, mesenteric superior artery, celiac artery and the portal vein:
  - Creating VR or AR 3D models of preoperative imaging may lead to more accurate planning and surgery;
- Co-registration of preoperative imaging with intraoperative ultrasonography:
  - Due to breathing and subsequent deformation of the organ this remains challenging;

- The challenge of determining known lesions in follow-up images, for monitoring purposes:
    - Early tumor recurrence may be hard to identify on current anatomical imaging modalities such as CT and MR imaging. Therefore, combining several imaging techniques could increase sensitivity and specificity for the detection of residual disease and early recurrence;
- The limitations of RECIST tumor evaluation:
    - CT and MR imaging have several limitations, therefore the addition of PET-CT may be of significant value to more accurately assess tumor's response to neoadjuvant chemotherapy.

2.4.4 Outcomes and project results

The partners of HPB use case have mainly focused on the automatic segmentation and fusion of different medical image modalities to create 3D anatomical models to be able to 1) improve planning of surgical liver resection, 2) improve diagnostic interpretation of scans, 3) be able to detect early pancreatic tumor recurrence, 4) assess the vascular involvement of pancreatic tumors, 5) improve the planning and placement of liver ablation needles. The developed methods of each partner are combined and implemented for the resection of pancreatic tumors and the resection or ablation of liver tumors.

The bullet points mentioned in 2.4.3 concerning the quality of the scans (1); accuracy of assessment of distant and nodal metastases for treatment planning (2): interpretation of 2-dimensional scans (4); and the challenge of determining known lesions in follow-up images, for monitoring purposes (6) are mainly covered in an application which has been developed during the ASSIST project. The application can perform organ segmentation, blood vessel segmentation and tumor segmentation. Different modalities can be used as input (CT and MRI) and modalities can be combined with each other; different scan from the same time point, but also scan from different time points to combine information. The output from this software is used to create 3D models which can be combined with AR and VR. Currently the LUMC, submitted the software for approval to use the software in-house use for clinical patients.
Next also the co-registration of preoperative imaging with intraoperative ultrasonography (5) has been investigated.

The correct restaging after neoadjuvant chemotherapy (3) could not be worked on due to the absence of ground truth data. Fusing the data from histology with CT/MR data was too challenging due to the very deformable nature of this tumor tissue. Also the RECIST tumor evaluation could not be done due to the absence of PET data. No suitable PET tracer was available for this task.

Deep learning segmentation
A robust approach in multimodality fusion is to isolate the organ of interest such as the liver and pancreas. This could be achieved by manual tracing but deep learning models were developed for the automatic delineation of both organs.

Quantib and the LUMC jointly created a deep learning model for the automatic segmentation of the liver using federated learning. The liver is automatically delineated

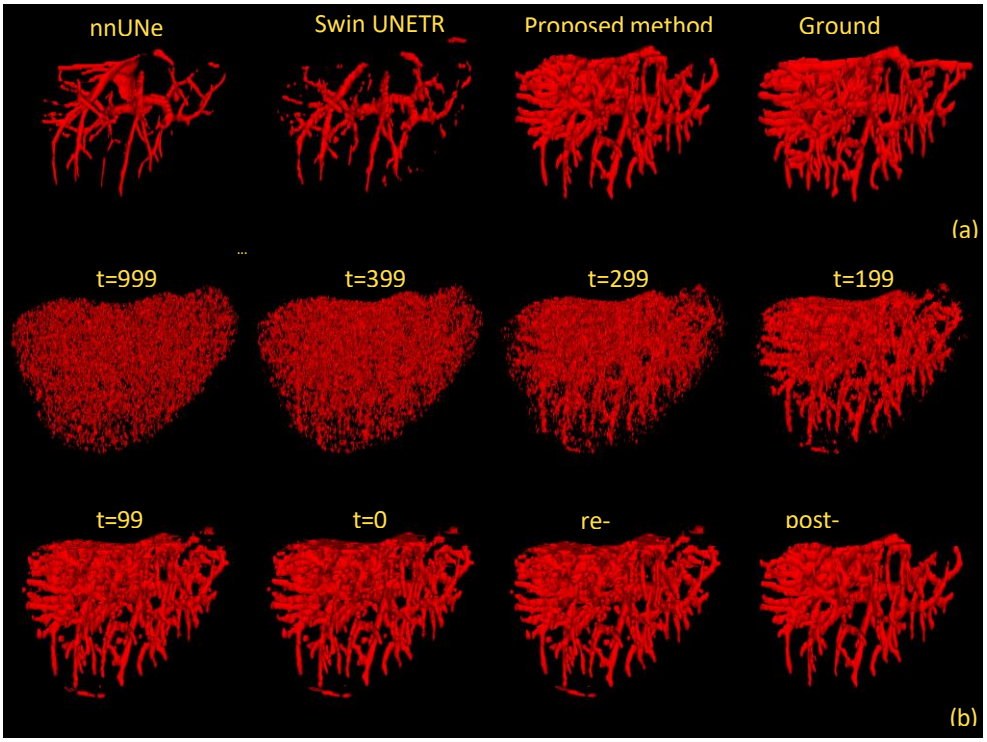

Figure 23: (a) Comparison of different methods for vascular tree detection. (b) Different iterations in the tree detection process using a diffusion model.

in a scan with contrast in the arterial tree and a scan with contrast in both the hepatic and portal venous trees to create a region-of-interest. An automatic co-registration algorithm uses these regions to automatically fuse the models of the vascular trees into one 3D model used to plan surgical liver resection. This model shows the distance between the tumor demarcations with respect to the vascular trees. A novel deep learning model was designed for the automatic detection of a vascular tree in the liver (Figure 23).

Similarly, deep learning models were developed to automatically delineate the pancreas in CT data and on MR imaging sequences using a continuous learning pipeline. The model improved its detection with each iteration (Table 1).

Table 1: Improvements in the continuous learning model for pancreas segmentation.

Continuous learning	**Batch 1**	**Batch 2**	**Batch 3**
Model 0	0.810	0.729	0.710
Model 0 pre-trained	0.822	0.783	0.716
Model 1	-	0.86	0.848
Model 2	-	-	0.882

Multimodality fusion

The final model was used again to delineate the pancreas in 3D in MR data and fuse a CT scan with the MR scan of the same patient for a combined visualization of tumor location and delineation (Figure 24).

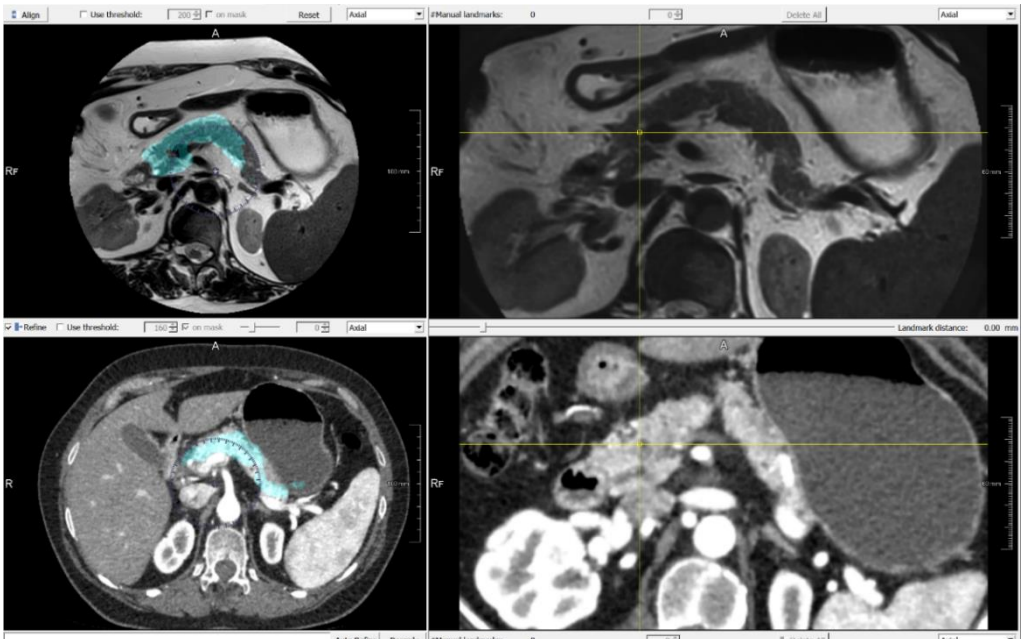

Figure 24: Image fusion of a MR scan (top row) and a CT scan (bottom row) in which an overlay (cyan) of the pancreas is projected on top of the other modality.

The same fusion approach can be used to combine baseline and follow-up MR scans for easier identification of early tumor recurrence.

Vascular involvement

The multimodality fusion of the preoperative scans improves interpretation but more detailed measurements could be obtained from a 3D model. The automatic pancreas delineations are used to create 3D surface models of the target organs such as the liver, pancreas but also the vascular structures. These models are used to quantify the circular involvement of blood vessels surrounding the pancreas (Figure 25). These quantifications are crucial for determining the resectability of a pancreas tumor as described in the guidelines from the Dutch Pancreatic Cancer Group.
Experiments were conducted to measure the effects of using a stereoscopic medical display from Barco to support surgical resection planning. There were no significant differences between using a monoscopic and stereoscopic view of the 3D model but there was a strong preference of the surgeons for using the stereoscopic view.

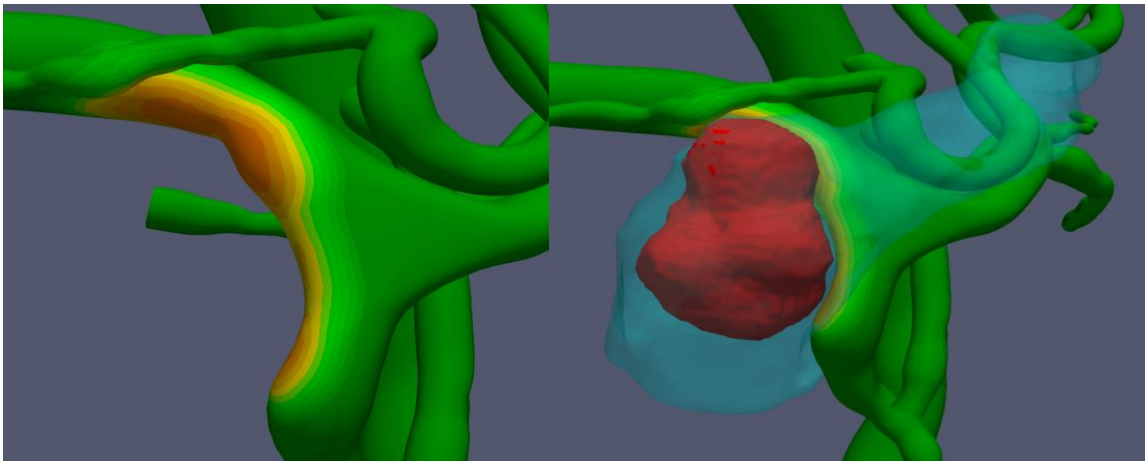

Figure 25: 3D model of the vascular involvement of a pancreas (transparent cyan) tumor (red). The distance between the tumor and vasculature is color-coded on the vessel. Green: >4 cm, yellow: 3-4 cm, and orange: 0-3 cm.

Liver ablation

The treatment of primary and secondary liver metastases can be performed by a thermal ablation procedure in which a needle is inserted to heat and destruct tumor tissue. The planning and placement of a needle requires a lot of experience to avoid nearby vascular structures. A virtual environment was made by Lifelike in which the 3D surface models of the liver, vascular structures and other relevant anatomical structures an integrated in order to simulate a needle placement procedure. Additionally, the needle planning software from the LUMC provided the actual final needle locations for the three target tumors (Figure 27).
This virtual environment was extended with a haptic feedback device from the University of Twente to create a more realistic experience when guiding the needle into the target tumor. The haptic device simulates the puncture of skin, liver parenchyma and tumor to approximate the real procedure.

Unlike in a static virtual simulation, breathing motion could prevent accurate insertion and placement of an ablation needle. A deep learning motion model was trained to capture the movements of the chest of a patient and correct for the location of insertion. Furthermore, ultrasound image navigation is used to verify if the needle has reached the target tumor. These images can be simulated using the respiratory motion model and used as surrogate signal to accurately predict the current location of the liver (Figure 26).

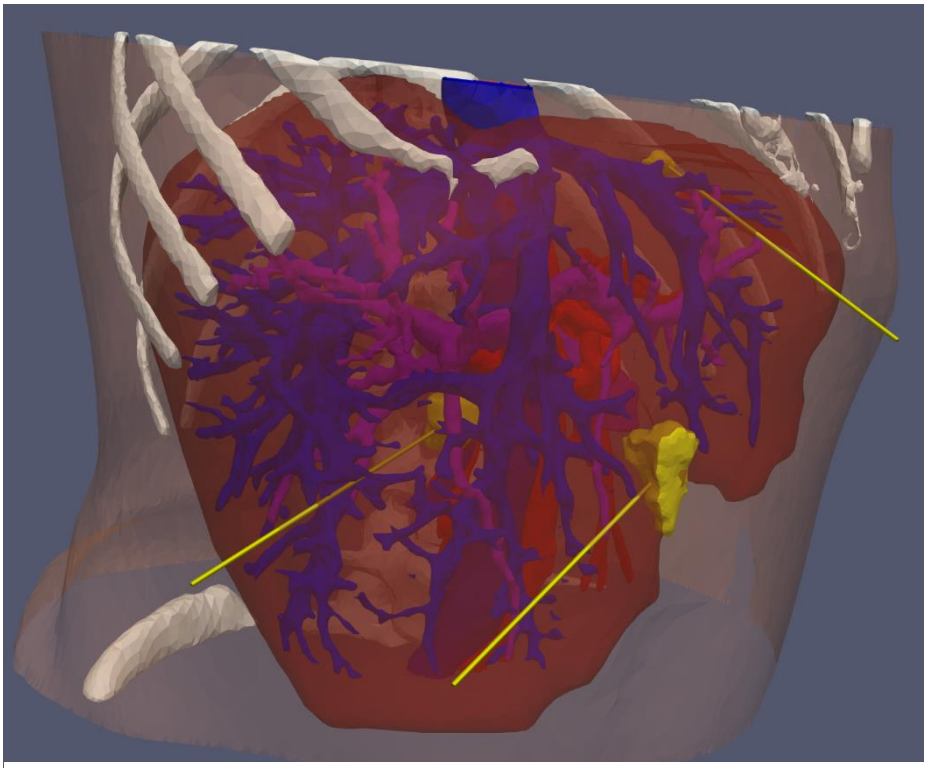

Figure 27: A virtual environment to simulate three needle placements to treat three tumors (yellow). With the vascular structures (blue and pink) within the liver (brown).

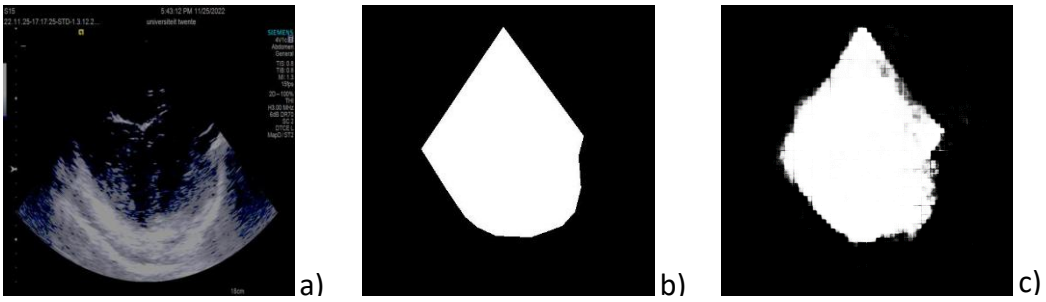

Figure 26: Needle placement is image guided by a) ultrasound images in which a b) liver mask has to be detected. A deep learning model is also able to predict this liver mask c) from a personalized breathing motion model.

2.5 Prostate enlargement

Owner: Fortearge – Serdar Sultanoglu / Mustafa Kemal

2.5.1 Introduction

Prostate enlargement, also called Benign prostatic hyperplasia (BPH), is a noncancerous increase in size of the prostate gland. (BPH), proliferation of the glandular and stromal tissue in the transition zone of the prostate, results in lower urinary tract symptoms (LUTS) and bladder outlet obstruction.

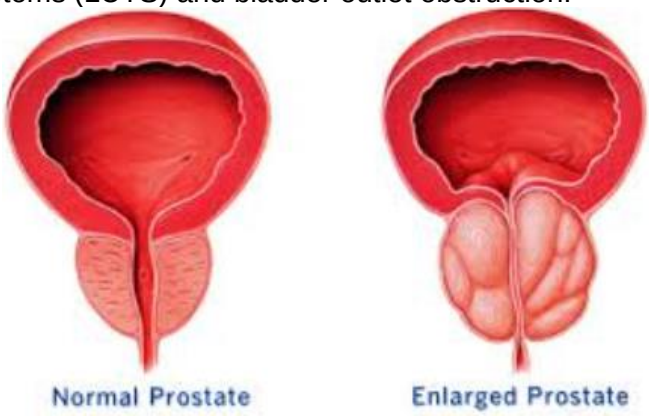

Figure 28 Normal vs Enlarged Prostate (A1, 2014)

The prevalence increases with age and 25% of men older than 70 years old have moderate to severe LUTS that effect their quality of life (QoL). About 105 million men are affected by BPH globally. It typically begins after the age of 40. Half of males age 50 and over are affected. After the age of 80 about 90% of males are affected.

A wide variety of medical and surgical options are available for the management of BPH with LUTS. In patients with moderate to severe LUTS refractory to medical management more invasive treatments are considered. Transurethral resection of the prostate (TURP) and open prostatectomy (OP) are the gold standard treatment methods for prostate glands of 30-80 cm^3 and ≥ 80 cm^3 respectively. However, these procedures have considerable morbidity rates including retrograde ejaculation, erectile dysfunction, urethral stricture, urinary retention, transfusion requirement and incontinence. Also in patients with existing comorbidities, increasing age and large prostate volume the complication rates are higher and hence the eligibility for surgical therapies are limited.
The primary goal of BPH treatment is to prevent or reverse urinary complications by improving LUTS.
Medical and surgical options are available; however, these procedures have considerable morbidity rates. Prostate artery embolization (PAE) has emerged as a minimal invasive treatment method which has a lower risk of urinary incontinence and sexual side effects.
The PAE procedure involves intra-arterial delivery of embolic materials to block the blood vessels supplying the hypertrophied transitional zone in the prostate gland.
In order for the PAE treatment to be successful, an in-depth analysis of the patient should be made before the procedure. In order for the procedure to be technically successful, accurate determination of the anatomy of the prostate arteries and adequate embolization of the target are required. This procedure should avoid non-target embolization (NTE) to other tissues, soft tissue of the bladder and rectum and penis, and other critical structures in the pelvis.

2.5.2 Clinical state of the art

Lifestyle changes and behavioural interventions are used to treat BPH in patients with mild symptoms. When the treatment does not work, medical means are used. Medical treatments that can be used to treat Alpha-blockers, 5-alpha reductase inhibitors, anticholinergics, and phosphodiesterase inhibitors include pills, injections, or patches. Many patients with BPH also have other health problems that make their LUTS worse. Some patients experience a series of serious adverse events, including irreversible sexual dysfunction, mood changes, and neurological and cognitive complaints that persist despite drug discontinuation. There are some limits to how much compliance people have with medical treatment, with 10% to 30% of people meeting treatment goals after one year. 25% of patients do not respond to medical treatment, especially those with major glands at baseline. Some medical treatments have little effect, making patients turn to surgery as their only recourse. This can be problematic because surgery is often less effective and can lead to bad side effects. (Gabr, 2021)

Surgical treatments that have developed over time include steam thermotherapy, prostate urethral lift, prostate ablative treatments (for example, monopolar transurethral resection of the prostate [M-turp], bipolar transurethral resection of the prostate [B-turp], transurethral electrovaporisation of the prostate [Tuvp], photoselective evaporation of the prostate) [Pvp], Holmium laser laser simple prostatectomy plus enucleation of the prostate [Holep] and thulium laser enucleation of the prostate [Thulep]). Surgical treatments have limitations, such as the need for general anaesthesia, foley catheterization, and a high rate of postoperative sexual dysfunction. There is variability in the success rates of surgical treatments for prostate cancer, depending on the size of the prostate gland. (Gabr, 2021)
A wide variety of medical and surgical options are available for the management of BPH with LUTS. In patients with moderate to severe LUTS refractory to medical management more invasive treatments are considered. Transurethral resection of the prostate (TURP) and open prostatectomy (OP) are the gold standard treatment methods for prostate glands of 30-80 cm^3 and ≥ 80 cm^3 respectively. However, these procedures have considerable morbidity rates including retrograde ejaculation, erectile dysfunction, urethral stricture, urinary retention, transfusion requirement and incontinence. Also in patients with existing comorbidities, increasing age and large prostate volume the complication rates are higher and hence the eligibility for surgical therapies are limited.
Prostate artery embolization (PAE) has emerged as a minimal invasive treatment method for the management of LUTS attributed to BPH. Although in the literature many data consisting of retrospective cohorts and few prospective studies exist, PAE has still not found its place in urological guidelines. FDA at the US recently approved PAE as an alternative treatment for LUTS related to BPH.
When considering PAE the technique is the challenging part requiring experience in recognizing prostatic arteries and avoiding non target embolization. As male internal iliac anatomy is prone to variations so are prostatic arteries which they can vary in origins, number. Besides, usually during treatment, cone beam CT is required especially with less experienced operators/angiographers. Many different protocols exist among centers for workup before the procedure to recognize and plan treatment including pre-operative CT imaging, MR imaging or no pre-imaging at all.

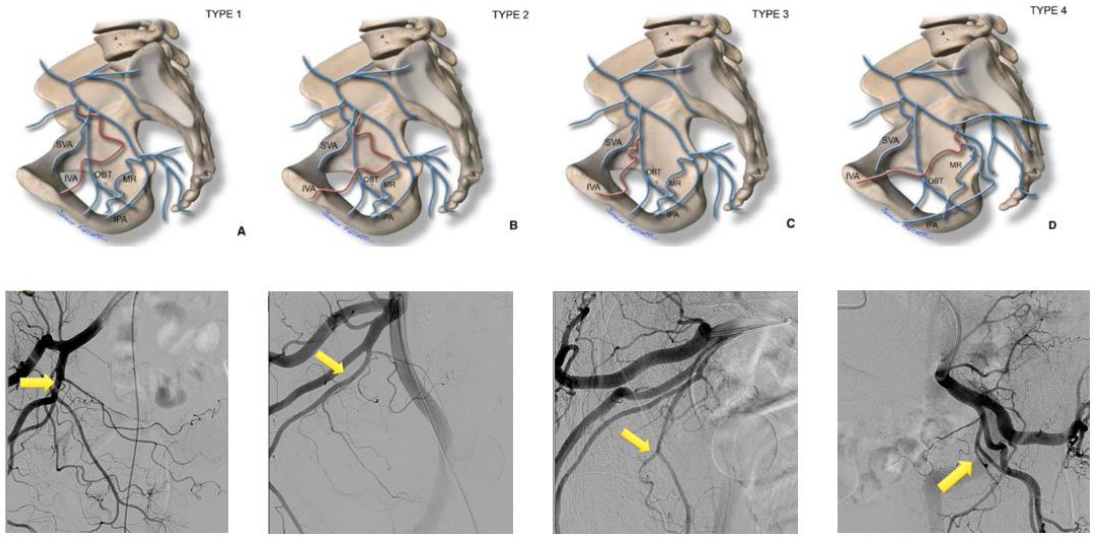

Figure 29 Variations in prostatic arteries

Pre-treatment non-contrast CT usually contributes little to the evaluation of prostate gland ultrasound or MRI. However, some clinicians wish to obtain a preprocedural computed tomography angiogram (CTA) to assess the extent of iliofemoral atherosclerosis and prostate artery anatomy to plan treatment. The reason is the data obtained that this technique will reduce the procedure time.

Pre-treatment computed tomography angiography is an imaging technique that can help identify prostate arteries and help plan prostate-artery embolization (PAE). The specificity of artery identification may decrease by 59% because of imaging protocols/parameters. A higher sensitivity to the magnetic resonance-inflationary pulse was found. *(Carnevale FC, 2020)* To identify the vascular patterns, an arterial CT angiography scan could be performed (2 mL/sec, with 4-6 seconds delay). Careful analysis of proximal cone-beam computed tomography (CBCT) datasets can identify arteries feeding the gland and other nontarget vessels. Segmentation of the pelvic and prostate vasculature and arteries of interest, both gland feeders and nontarget vessels, allows creating a 3D model that can be used for advanced guidance. *(Carnevale FC, 2020)*To identify the vascular patterns, an arterial CT angiography scan could be performed (2 mL/sec, with 4-6 seconds delay).

Other most common tool in cone-beam CT angiography which is obtained during the DSA for PAE. So, the patient is already on the table for PAE and CBCT is used as a complimentary imaging tool to identify the prostatic artery or other non-target branches Careful analysis of proximal cone-beam computed tomography (CBCT) datasets can identify arteries feeding the gland and other nontarget vessels.

Segmentation of the pelvic and prostate vasculature and arteries of interest, both gland feeders and nontarget vessels, allows creating a 3D model that can be used for advanced guidance. *(Carnevale FC, 2020)*

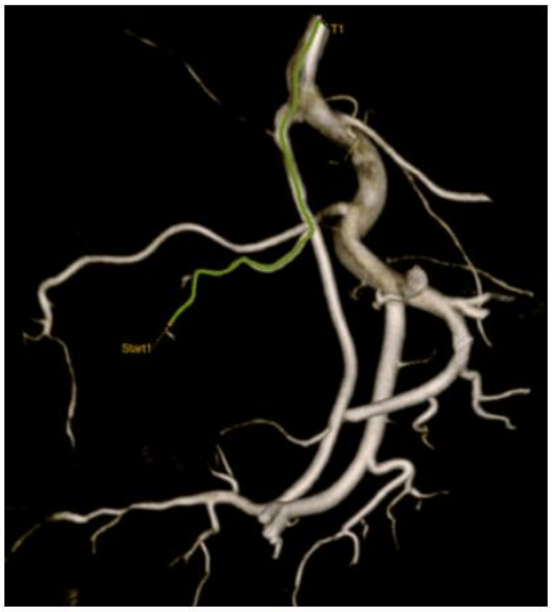

Figure 30 A 3D reconstruction model of the left internal iliac artery branches was automatically segmented. The prostate artery and catheterization path are highlighted in green. (Carnevale FC, 2020)

Virtual 3D anatomical data can be obtained using augmented reality and AI-based CT, CBCT or MRI. This is the fusion of real-world 2D visual images, creating a virtual device trajectory superimposed on the visual surface anatomy. Theoretically, accurate navigation can be achieved without the need for fluoroscopy. *(Gurgitano M, 2021)*

Thanks to the integrated matching AI software, automatic landmark recognition and motion compensation can be enabled using reference markers linked by a computer algorithm. This system can be applied in lesion targeting/localization, spinal/paraspinal injections, arthrograms, tumour ablation, bone biopsies and more recently minimally invasive surgical procedures. *(Gurgitano M, 2021)*

2.5.3 Workflow inefficiencies and bottlenecks

- Complexity of the technique
  - When considering PAE, the challenging part in this technique requires experience in recognizing prostatic arteries and avoiding non target embolization. As male internal iliac anatomy is prone to variations so are prostatic arteries which they can vary in origins, number.
  - Non-target embolization is a potential drawback of the procedure.
- Need for expensive medical devices
  - Pretreatment CTA is more accessible
  - Usually during treatment, cone beam CT is required especially with less experienced operators/angiographers. Although not every IR has it with angio units, it is becoming a must have tool with DSA in the last 10 years.
- Longer operation time
  - The shorter the operation time, the higher the patient satisfaction. During the procedure, the physician's time to find the target artery increases the operation time.

- Excess radiation exposure
  - Since automatic artery identification cannot be performed in the current situation, the patient is examined with more imaging techniques.
- The clinician should combine many data before the procedure
  - While making a diagnosis, many tests applied to the patient should be combined and understood by the clinician. This is a difficult procedure for the clinician. If the clinician is given the fusion of all image data, it becomes easier for the clinician to diagnose and plan treatment.
- Late diagnosis
  - The clinician's difficulty in combining many data affects the time to diagnosis. Early diagnosis is extremely important in terms of planning the treatment process of the patient.
- Experienced physician requirement
  - Prostatic Artery Embolization is a difficult process, so it is not possible for all clinicians to perform it. Due to the difficulties mentioned in the previous articles before and after the treatment, experienced doctors are expected to perform the treatment.

2.5.4 Outcomes and project results

The Vascular Navigation Assistant System (V-NAS) has been designed to transform prostate artery embolization (PAE) into a more accurate, efficient, and accessible procedure. Through real-time image processing, V-NAS minimizes radiation exposure and contrast agent use while enhancing procedural precision, ultimately improving outcomes for patients with benign prostatic hyperplasia (BPH).

General Objectives and Goals
The primary objective of this project is to improve the safety and effectiveness of PAE, a minimally invasive treatment for BPH. V-NAS aims to assist physicians in navigating the complex vascular anatomy required for embolizing the prostatic artery by providing real-time guidance. This system minimizes the need for repeated imaging attempts and reduces patient exposure to both radiation and contrast agents, improving procedural efficiency and accuracy.

Through the development of V-NAS, the project seeks to:

- Improve the precision of PAE by helping physicians quickly and accurately identify the prostatic artery.
- Reduce the use of contrast agents and limit radiation exposure, benefiting patients who may have kidney issues or are at risk of radiation-induced complications.
- Shorten procedural times, making PAE more accessible to less experienced interventional radiologists and improving patient outcomes by reducing the invasiveness of treatment.

Developed Methods and Solutions
V-NAS operates by processing angiographic images in real time, analyzing each contrast injection to offer the physician two critical types of guidance:

1. Optimal Projection Angles: By recommending the best imaging angles, the system helps avoid vessel overlap, ensuring that vascular structures are clearly visible. This reduces the likelihood of error and the need for repeated imaging attempts.

2. Targeted Contrast Agent Administration: V-NAS suggests the ideal injection points for contrast agents, minimizing the amount required while still ensuring high-quality imaging. This is especially beneficial for patients with renal impairments.

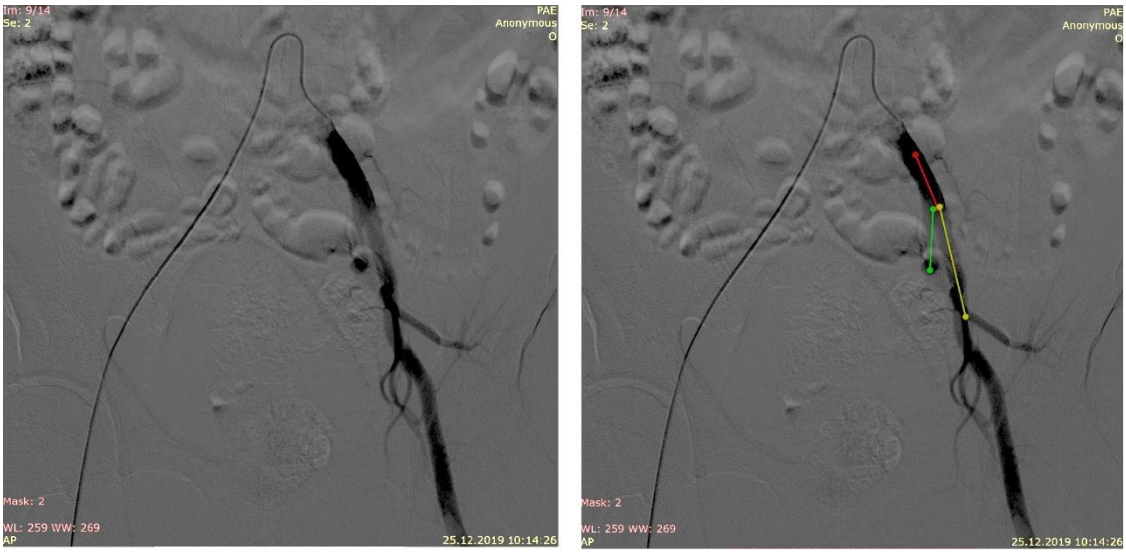

Figure 31 Internal and external iliac arteries identified before and after V-NAS guidance during PAE

The system assists physicians in navigating key anatomical landmarks during PAE, from the femoral artery through the internal iliac artery to the prostatic artery. This real-time guidance reduces the guesswork involved in the procedure, leading to faster, safer outcomes.

Technological and Scientific Contributions
V-NAS provides several technological and scientific advancements that significantly enhance PAE procedures:

- **Real-Time Feedback:** The system processes angiographic images in real time, delivering actionable insights that allow physicians to adjust their approach dynamically throughout the procedure. This real-time analysis minimizes errors and improves procedural outcomes.
- **Reduced Radiation and Contrast Exposure:** By reducing the number of repeated imaging attempts and optimizing contrast agent usage, V-NAS helps to significantly lower radiation exposure for both patients and medical staff. The targeted administration of contrast agents also reduces the risk of adverse reactions, benefiting patients with contrast sensitivities.
- **Enhanced Anatomical Visualization:** V-NAS recommends projection angles that prevent vessel overlap, making it easier for physicians to accurately identify the prostatic artery and surrounding structures. This contributes to a higher success rate in embolization procedures and reduces complications like non-target embolization.

Applications and Results
Preliminary results from clinical trials demonstrate that V-NAS improves the efficiency and safety of PAE procedures in several ways:

- **Reduced Procedure Time:** By providing real-time guidance on contrast injection and imaging angles, V-NAS has been shown to reduce procedural time by up to 30%. This shorter procedure duration improves patient comfort and reduces the strain on medical teams.
- **Minimized Use of Contrast Agents:** With its targeted recommendations for contrast administration, V-NAS decreases the overall use of contrast agents, improving safety, particularly in patients with kidney problems or those at risk for contrast-induced complications.
- **Increased Procedural Accuracy:** The system helps physicians accurately identify the prostatic artery and avoid vessel overlap, which in turn reduces the likelihood of complications and improves overall outcomes.
- **Wider Physician Adoption:** V-NAS makes PAE more accessible to a broader range of physicians, particularly those with less experience, by offering detailed, step-by-step guidance through complex vascular structures.

Limitations and Challenges:
While V-NAS has demonstrated significant potential, several challenges remain:

- **Compatibility with Imaging Systems:** The system must be tested and calibrated to work with a wide variety of imaging systems used in different clinical environments. Ensuring seamless integration with existing angiographic equipment is crucial to its widespread adoption.
- **Dependence on Image Quality:** The accuracy of V-NAS recommendations is dependent on the quality of the angiographic images it analyzes. Poor image resolution or patient movement during the procedure may affect the system's ability to provide accurate guidance.
- **Real-Time Performance:** The system's ability to process images and deliver feedback in real time is computationally demanding. Ensuring that V-NAS maintains high performance even in extended or complex procedures is essential to its success.
- **Training and Implementation:** Successful adoption of V-NAS requires proper training for physicians and staff. Integration into existing clinical workflows may be challenging, particularly in facilities with limited resources or less experience in advanced imaging technologies.

Future Work and Development Areas
The development of V-NAS will continue to focus on overcoming these limitations while expanding its capabilities:

- **Wider Integration and Compatibility:** Future work will aim to enhance the system's compatibility with a broader range of imaging systems and clinical workflows, ensuring that it can be used across diverse healthcare settings.
- **Optimization of Real-Time Performance:** Efforts will focus on refining the system's real-time processing capabilities, improving both speed and accuracy to ensure consistent performance in complex procedures.
- **Application to Other Procedures:** The core technologies behind V-NAS can be adapted to other vascular procedures, such as uterine artery embolization, peripheral artery interventions, and cardiac catheterization. Expanding its utility to these fields will increase its value in interventional radiology.
- **Artificial Intelligence and Explainability:** Future iterations of V-NAS may include advanced explainability features, using explainable AI (XAI) techniques

to provide greater transparency in the system's decision-making process. This will allow physicians to better understand and trust the system's recommendations.

- **Clinical Validation and Expansion:** Wider clinical trials in diverse healthcare environments will be conducted to validate the effectiveness of V-NAS in reducing procedural times, minimizing radiation exposure, and improving patient outcomes. These trials will be crucial for securing regulatory approvals and ensuring the system's broader adoption in clinical practice.

By continuously refining and expanding V-NAS, the project aims to set a new standard in the safe and effective performance of minimally invasive procedures, not just in PAE, but across a variety of vascular interventions.

3 Conclusions

This document gives an overview of the clinical disease areas addressed in the ASSIST project and describes the updated State of the Art for the clinical procedures targeting these diseases. Generally, complexity in diagnosis and treatment steps is recognized as a common challenge and has been addressed in the project in all use cases.

Automated image segmentation, enabled by Deep Learning, has delivered valuable workflow improvements in terms of higher accuracy, less manual actions, and shorter procedure time, in all clinical use cases.

4 REFERENCES

Abramian, D., Eklund, A., & Özarslan, E. (2023). Super-resolution mapping of anisotropic tissue structure with diffusion MRI and deep learning. *bioRxiv*, 2023-04.

Akbar, M.U., Larsson, M., Blystad, I., & Eklund, A. (2024). Brain tumor segmentation using synthetic MR images-A comparison of GANs and diffusion models. *Scientific Data*, *11*(1), 259.

Akbar, M.U., Wang, W., & Eklund, A. (2023). Beware of diffusion models for synthesizing medical images--A comparison with GANs in terms of memorizing brain tumor images. *arXiv:2305.07644*.

Boito D., Herberthson M., Dela Haije T.C.J., Blystad I., Özarslan E. (2023) Diffusivity-limited q-space trajectory imaging. Magnetic Resonance Letters, 3:187–196.

Boito, D., Özarslan E. (2023) Q-space trajectory imaging with positivity constraints: a machine learning approach. Proc Intl Soc Mag Reson Med, 31, Toronto, p. 3780.

Ekmefjord, M., Ait-Mlouk, A., Alawadi, S., Åkesson, M., Singh, P., Spjuth, O., ... & Hellander, A. (2022, May). Scalable federated machine learning with fedn. In *2022 22nd IEEE International Symposium on Cluster, Cloud and Internet Computing (CCGrid)* (pp. 555-564). IEEE.

Herberthson M., Boito D., Dela Haije T.C.J., Feragen A., Westin C.F., Özarslan E. (2021) Q-space trajectory imaging with positivity constraints (QTI+). NeuroImage, 238:118198.

Shusharina, N., & Bortfeld, T. (2021). Glioma Image Segmentation for Radiotherapy: RT targets, barriers to cancer spread, and organs at risk (GLIS-RT) [Data set]. The Cancer Imaging Archive. https://doi.org/10.7937/TCIA.T905-ZQ20

A1, F. (2014).

Béjot, Y. B. (2016). Epidemiology of stroke in Europe and trends for the 21st century.

Burduja, M. I. (2020). Accurate and Efficient Intracranial Hemorrhage Detection and Subtype Classification in 3D CT Scans with Convolutional and Long Short-Term Memory Neural Networks. *Sensors* (s. 5611). içinde

Caceres, J. &. (2012). Intracranial Hemorrhage. *Emerg Med Clin North Am* (s. 771-794). içinde

Carnevale FC, d. A. (2020). Prostatic Artery Embolization: Equipment, Procedure Steps, and Overcoming Technical Challenges. *Techniques in Vascular and Interventional Radiology*.

Clinic, M. (tarih yok). *Stroke - Diagnosis and treatment - Mayo Clinic.*

Fernando, S. M. (2018). Outcomes and Costs of Patients Admitted to the ICU Due to Spontaneous Intracranial Hemorrhage. *Critical Care Medicine* (s. 395-403). içinde

Gabr, A. S. (2021). Contemporary Review of Prostate Artery Embolization for the Treatment of Benign Prostatic Hyperplasia: Technical Considerations and Long-Term Outcomes. Advances in Clinical Radiology.

Gurgitano M, A. S. (2021). Interventional Radiology ex-machina: impact of Artificial Intelligence on practice. *La radiologia medica*.

Hosseini, M. J. (2017). A Mobile Geo-Communication Dataset for Physiology-Aware DASH in Rural Ambulance Transport. *Proceedings of the 8th ACM on Multimedia Systems Conference.*

Hssayeni, M. C.-k. (2020). Intracranial Hemorrhage Segmentation Using a Deep Convolutional Model. *Data* (s. 14). içinde

IARC. (2018). *Latest global cancer data:.* World Health Organization.

Kim, C. H. (2021). Clinical usefulness of deep learning-based automated segmentation in intracranial hemorrhage. *Technology and Health Care* (s. 881-895). içinde

Mayo. (2022). *Lung Cancer.*

Mirza, S. &. (2017). Neuroimaging in Intracerebral Hemorrhage. *Hemorrhagic Stroke*.

Patel, A. S. (2019). *Intracerebral Haemorrhage Segmentation in Non-Contrast CT.* Scientific Reports.

Prevention, U. C. (2017). *CDC 2017: 'Screening for Lung Cancer – 10 States.*

Qdaisat, A. Y. (2022). Characteristics and Outcomes of Intracranial Hemorrhage in Cancer Patients Visiting the Emergency Department. *Journal of Clinical Medicine*, 643.

Siegel, R. L. (2021). Cancer Statistics. *CA: A Cancer Journal for Clinicians*.

Society, A. C. (2019). *What is Lung Cancer.*

Unnithan AKA, M. P. (2022). Hemorrhagic Stroke. *StatPearls [Internet]*.

van Dam, M. A.-O.-F.-J. (2021). Overview and Future Perspectives on Tumor-Targeted Positron Emission Tomography and Fluorescence Imaging of Pancreatic Cancer in the Era of Neoadjuvant Therapy. *Cancers*.

Ye, H. G. (2019). Precise diagnosis of intracranial hemorrhage and subtypes using a three-dimensional joint convolutional and recurrent neural network. *European Radiology*, 6191-6201.

Yousufuddin, M. M. (2020). Initial and subsequent 3-year cost after hospitalization for first acute ischemic stroke and intracerebral hemorrhage. *ournal of the Neurological Sciences*.

Karras, T., Aittala, M., Hellsten, J., Laine, S., Lehtinen, J., & Aila, T. (2020). Training generative adversarial networks with limited data. Advances in neural information processing systems, 33, 12104-12114.

Liu, B., Zhu, Y., Song, K., & Elgammal, A. (2020, October). Towards faster and stabilized gan training for high-fidelity few-shot image synthesis. In International conference on learning representations.

Karras, T., Aittala, M., Laine, S., Härkönen, E., Hellsten, J., Lehtinen, J., & Aila, T. (2021). Alias-free generative adversarial networks. Advances in neural information processing systems, 34, 852-863.

Zhu, J. Y., Park, T., Isola, P., & Efros, A. A. (2017). Unpaired image-to-image translation using cycle-consistent adversarial networks. In Proceedings of the IEEE international conference on computer vision (pp. 2223-2232).

Wang, X., Shen, T., Yang, S., Lan, J., Xu, Y., Wang, M., Zhang, J., & Han, X. (2021). A deep learning algorithm for automatic detection and classification of acute intracranial hemorrhages in head CT scans. NeuroImage: Clinical, 32, 102785. https://doi.org/10.1016/j.nicl.2021.102785